Gao, Y., W.H. Ali, C. Foucart, C. Mirabito, P.J. Haley, Jr., and P.F.J. Lermusiaux, 2026. 3DSeaVizKit: An Interactive Spatiotemporal Visualization Toolkit for Ocean Data. Ocean Modelling, sub-judice.

3DSeaVizKit: An Interactive Spatiotemporal Visualization Toolkit for Ocean Data

Youran Gao[a], Wael H. Ali[a], Corbin Foucart[a], Chris Mirabito[a], Patrick J. Haley, Jr.[a], Pierre F.J. Lermusiaux[a,]

[a]*Massachusetts Institute of Technology, 77 Massachusetts Ave., Cambridge, MA 02139, USA*

Abstract

Scientific understanding, prediction, and communication to stakeholders are common objectives of ocean simulations and observing campaigns. Achieving these objectives can be greatly facilitated by advanced tools for exploring dynamic three-dimensional ocean data. Many scientific visualizations of spatiotemporal simulations rely on static two-dimensional representations that omit one or more spatial dimensions, potentially obscuring important features and relationships. A toolkit capable of creating coherent three-dimensional visualizations of ocean processes should move beyond isolated two-dimensional views and support the exploration of increasingly high-resolution simulations and large multidisciplinary observational data sets. In this work, we present 3DSeaVizKit, a visualization toolkit that processes multidisciplinary oceanographic data in a modular and computationally efficient manner to create portable, web-based, interactive 3D visualizations. Built upon the Plotly JavaScript library, the toolkit enables exploratory analysis of complex ocean fields directly within a web browser. We provide a software pipeline tailored to the computational demands of multivariate 3D ocean visualization and demonstrate its utility for revealing transport pathways, coherent structures, circulation features, biogeochemical-acidification interactions, subduction dynamics, and forecast uncertainties in high-resolution ocean simulations. The toolkit supports scalar fields such as temperature, salinity, and biogeochemical tracers; vector fields such as velocity and vorticity; and Lagrangian products including trajectories, flow maps, and coherent structures. Applications include the visualization of the Loop Current system and eddy interactions in the Gulf of Mexico, subduction processes and forecast uncertainties in the Alboran Sea, coupled biogeochemical and ocean-acidification dynamics in Massachusetts Bay, and transport pathways and coherent structures around Nantucket and Martha's Vineyard.

Keywords:
Interactive 3D visualization, Ocean simulation, Ocean dynamics, Transport pathways, Lagrangian coherent structures, Biogeochemical dynamics, Forecast uncertainties

Email address: pierrel@mit.edu (Pierre F.J. Lermusiaux)

1. Introduction

A primary value of an ocean simulation or observing campaign lies in the scientific understanding and predictions it enables, and in the communication of these results to stakeholders and society. However, the effective scientific visualization of oceanographic data is an often-neglected but critical component in understanding ocean phenomena. Indeed, given the large computational costs and software development time associated with running numerical ocean simulations, the utility of developing an effective visualization tool is substantial. Efficient, interactive, three-dimensional (3D) visualization of spatiotemporal data would aid researchers and professionals in interpreting and analyzing ocean data. Such visualizations could support diverse applications, including shipping [1], disaster management [2], off-shore oil operations [3], or aquaculture [4].

Visualization of oceanographic data is not without its challenges: simulations and data sets are often large, highly multivariate, and may contain uncertainties and discontinuous data [5, 6, 7, 8, 9, 10, 11, 12]. These complexities necessitate a visualization toolkit capable of handling multi-dimensional, multiresolution products. It is also important to consider the compromise between visual resolution and speed when designing a software solution, as any visualization becomes ineffective—or worse, deceptive—if too much data is lost in down-sampling prior to visualization [5, 13, 14]. On the other hand, it is of practical importance to be able to deliver visualizations quickly and efficiently. The resultant resolution-speed trade-off is a delicate balance requiring careful treatment [15].

The common approach to oceanographic data visualization involves plotting multiple 2D lateral or depth-wise cross-sections, whereby users manually select cross-sections and times for plotting at the software level, and are left to interpret the static output plots [16, 17, 18]. Such an approach requires the user to reconstruct 3D structures from 2D cross- and depth- sections, a process that can be time-consuming and require significant mental effort to infer the underlying dynamics. In contrast, employing 3D visualization can drastically improve the ease of interpretation, because the user can directly explore spatial relationships among multiple horizontal and vertical structures, rather than imagine a 3D data field from isolated 2D slices [5, 19]. Although 3D visualization may be computationally expensive, judicious application of state-of-the-art software and hardware techniques can increase responsiveness, and doing so creates new possibilities for visualizing flows and eddies between different depths [20]. Beyond improving interpretation, interactive 3D visualization can reveal transport pathways, vertical connectivity, the full variability of structures, and multiscale dynamical processes that are difficult to identify from separate two-dimensional maps and sections. Such capabilities are increasingly needed as ocean simulations and observing systems continue to grow in resolution, complexity, and dimensionality. Several 3D flow visualization tools, such as VisIt [21] and ParaView [22], have been established to address some of these needs. However, these general-purpose tools are not specifically designed for oceanographic workflows and often require substantial customization to support ocean-model grids,

oceanographic diagnostics, and exploratory analysis [5]. More recently, a few specialized 3D ocean data rendering tools have been developed, either as standalone [23, 24] or web-based software [25]. Some of these tools specialize in visualizing specific processes, e.g., biogeochemical and microbial processes near the seafloor [26], or are tailored to specific data systems [27]. For web-based tools, 3D visualization is computationally intensive, and methods have been proposed to improve rendering performance [14].

Another important feature for exploratory ocean visualization is interactivity, as it allows the user to select the field to visualize and the images to display, zoom into the areas of interest, and choose the time at which the specific ocean process is to be explored. Yet, such interactivity typically comes at a cost for loading and online processing of the data. These challenges have restricted such interactive tools for 2D visualization [28, 13]. Recent advances in graphics hardware have allowed extending these features for 3D visualization in meteorology and led to the development of interactive tools such as Met.3D [29], MEVA [30], and W3DX [31]. Additionally, interactive 3D flow visualization tools such as Vis5D [32] and VAPOR [33] have been used for ocean visualization.

In this work, we present 3DSeaVizKit as a software toolkit that simplifies the interpretation of ocean simulations through interactive 3D visualization while remaining computationally efficient and providing a responsive user experience. Our toolkit consists of a data pre-processing pipeline that supports operations on the computational grids and file formats widely used in oceanography and geosciences. The visualization suite makes extensive use of the Plotly JavaScript library [34] to implement various algorithms for plotting scalar, vector, and Lagrangian data using lines, maps, cross-sections, isosurfaces, trajectories, and streamtubes. The output visualization is served over the web, providing a seamless and intuitive graphical interface guiding the user throughout the 3D dynamic ocean data exploration. The new 3DSeaVizKit augments our previous contributions for high-performance visualization in ocean modeling, including our 2D interactive visualization tool, 2DSeaVizKit [13], and our NCAR Graphics and MATLAB-based tools for static visualization [35]. This paper develops and illustrates the features and capabilities of 3DSeaVizKit, emphasizing 3D analysis, exploratory studies, and interactive, dynamic real-time visualization. Building upon preliminary tests [35], we employ 3DSeaVizKit to visualize multiresolution multivariate ocean simulation outputs of the MIT MSEAS high-resolution probabilistic primitive equation modeling system [36, 37, 38, 39]. We demonstrate the use of the toolkit in four ocean applications spanning coastal transport, biogeochemical and acidification dynamics, Loop Current system evolution, subduction events, and forecast uncertainty quantification. These examples illustrate how 3DSeaVizKit can help reveal coherent structures, transport pathways, subduction phenomena, multiscale circulation features, coupled physical-biogeochemical processes, and forecast uncertainties that are difficult to infer from collections of static 2D views.

The principal contributions of this work are: (i) a computational pipeline for efficient web-based visualization of multivariate ocean data; (ii) interactive 3D visualization methods for scalar, vector, Lagrangian, and probabilistic ocean

products within a unified web-based framework; and (iii) demonstrations showing how such visualizations facilitate the analysis of 3D features, transports, circulations, subduction events, physical-biogeochemical processes, and uncertainty fields in realistic ocean applications. In §2, we discuss the underlying data and software pipeline employed by 3DSeaVizKit. In §3, we highlight the toolkit capabilities for visualizing the scalar, vector, and trajectory data. In §4 we describe the applications where 3DSeaVizKit is used to analyze ocean simulation outputs in real sea experiments. In §5, we provide a summary and conclusions.

2. Software pipeline

The 3DSeaVizKit visualization suite consists of a pre-processing pipeline that extracts and processes the ocean simulation outputs, and a graphical user interface (GUI) that produces interactive 3D visualizations over the web. The software pipeline is outlined in Figure 1. Further information about the ocean data, pre-processing steps, and GUI are provided next.

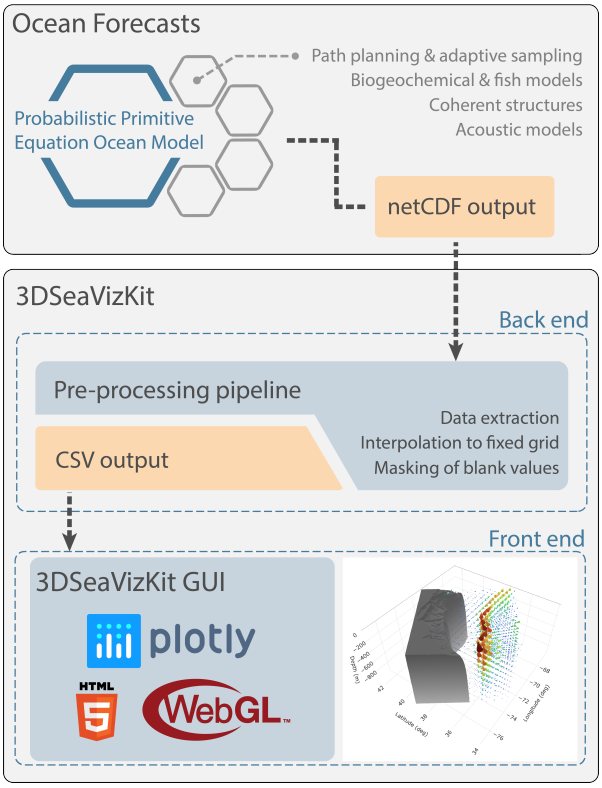

Figure 1: 3DSeaVizKit pipeline, showing the process of representing primitive equation (PE) ocean simulations and forecasts, converting outputs to 3D visualizations in the browser. The depicted sample output is a cone plot generated from a MSEAS velocity field simulation for the Gulf Stream, in the Middle Atlantic region.

2.1. MSEAS Model Input

The ocean fields used in our visualization cases are simulation outputs of the MIT MSEAS software [36, 39] written in netCDF files. They are represented by the "Ocean Forecasts" panel in Figure 1. The MSEAS software consists mainly of a nonlinear free-surface hydrostatic primitive-equation (PE) model, based on second-order structured finite volumes and configured with generalized-level vertical-coordinates and implicit two-way nesting [37, 39]. The software has different features which expand its capabilities to include nested data-assimilative tidal prediction and inversion [40], ensemble forecasting and data assimilation using the Error Subspace Statistical Estimation (ESSE) methodology [41, 42, 43], adaptive data assimilation, sampling and learning [44, 45, 46], biogeochemical modeling and environmental management [47, 48, 49], Lagrangian Coherent Structures (LCSs) [50, 51], planning for autonomous vehicles [52, 53], and underwater sound propagation [54, 55, 56, 15]. The MSEAS software has been used for forecasting the ocean fields and related products in many regions around the world. The visualization examples shown in this work are based on MSEAS real-time probabilistic forecasts and data-assimilative simulations completed for the following research projects and sea experiments: NSF "Advanced Lagrangian Predictions for Hazards Assessments" (NSF-ALPHA), "Bayesian Intelligent Ocean Modeling and Acidification Prediction Systems" (BIOMAPS), Gulf of Mexico (GOM) Loop Current System, and "Coherent Lagrangian Pathways from the Surface Ocean to Interior" (CALYPSO) initiative.

2.2. Data Pre-processing

The output netCDF files of the MSEAS ocean simulation are the inputs to the back-end of 3DSeaVizKit. Our Python pre-processing pipeline (second panel of Figure 1) utilizes several command-line utilities to transform the netCDF files into CSV files that can be easily served to the front-end via the web. These utilities allow the user to specify the ocean fields and time window of interest. The pre-processing pipeline also provides utilities for transforming the ocean data from a terrain-following grid (commonly used in atmospheric and ocean models) to a flat level grid (for fast 3D visualization, see Appendix A for details). Written with scalability in mind, the pre-processing pipeline allows the user to use any number of available processors for better performance.

2.3. Web-based Visualization

The GUI of 3DSeaVizKit (represented by the "Front End" panel in Figure 1) is a web-based tool that makes visualization of 3D ocean data feasible when serving data over the web. The toolkit makes extensive use of the JavaScript library Plotly [34]. Through Plotly's use of WebGL, 3DSeaVizKit is able to take advantage of the Graphics Processing Unit on the user's computer (when available), significantly improving client performance.

3DSeaVizKit provides the user with interactive tools for exploring 3D fields such as panning, zooming, and mouse-over display of data values. Additionally, the toolkit also has 3D-specific features such as turntable and orbital rotation,

interactively added cross and depth sections, and the ability to visualize the evolution of displayed quantities.

The web-based visualization toolkit loads data asynchronously to allow responsiveness while files load over the network in the background. Almost every aspect of the plotting is configurable by the user either through the use of JSON files or through the user interface. The portions of the data to be plotted, the configuration of the plotting parameters, or the aesthetic appearance of the visualization can all be customized without changes to the source code. The modular toolkit allows for multiple plot types to be displayed on a single visualization, giving the oceanographer greater flexibility and easier interpretation. The portability of a web-based tool also allows for interactive, exploratory data visualization through any web browser or on a mobile device.

3. Toolkit capabilities

To illustrate the capabilities and features of the toolkit, we will make extensive use of a 3D modification to the canonical idealized double-gyre flow field [57, 58, 59], where the velocity vector field is given as

$$\mathbf{v}(x,y,z,t) = \pi A \begin{pmatrix} -\sin(\pi f(x,t))\cos(\pi y) \\ \cos(\pi f(x,t))\sin(\pi y)\,\frac{\partial}{\partial x} f(x,t) \\ 2z(1-z)\left(z - \epsilon \sin\left(\frac{4\pi t}{T}\right) - \frac{1}{2}\right) \end{pmatrix}, \tag{1}$$

with $f(x,t) = \epsilon \sin(t/T)\, x^2 + (1 - 2\epsilon \sin(t/T))\, x$, $x \in [0,2]$, $y \in [0,1]$, $z \in [0,1]$, and $t \in [0,10]$.

This model serves as a simplification of a double-gyre pattern commonly seen in geophysical flows [57, 60, 61]. The case parameters used in this work are: $A = 1/10$, $\epsilon = 1/4$, and $T = 5/\pi$, and the resulting flow is time-dependent, consisting of two gyres expanding and contracting periodically in the x-direction [57]. For our numerical implementation, the model domain is discretized using $N_x = 200$, $N_y = 100$, $N_z = 100$, and $N_t = 50$ points.

3.1. Visualizing Scalar-valued Data

Models of the ocean make extensive use of purely scalar field quantities such as temperature, salinity, or any scalar component of vector fields, e.g. vertical vorticity, necessitating the need for effective visualization of these quantities as fully 3D fields.

3.1.1. Cross Sections and Depth Sections

3DSeaVizKit enables the user to place two-dimensional cross-sections of 3D scalar fields, as shown in Figure 2a. When a user selects a latitude, longitude, or depth cross-section to plot, the toolkit interactively renders a 2D pseudocolor plot at the specified latitude, longitude, or depth. Each 3DSeaVizKit figure portraying scalar-valued data allows for the addition of arbitrarily many cross sections in latitude, longitude, and depth, which are displayed at once. Figure

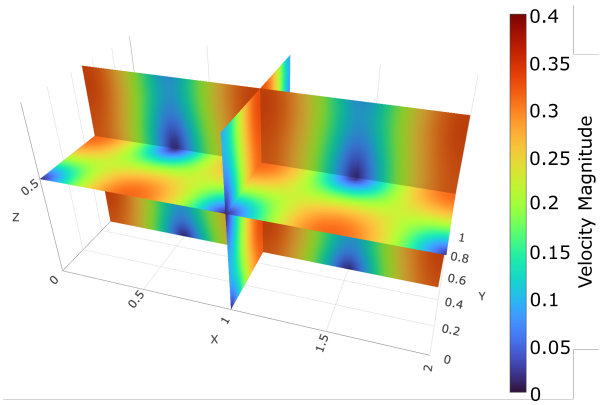

(a) Cross-sections of velocity magnitude for double gyre flow (1) at $x = 1$, $y = 0.5$, and $z = 0.5$, $t = 0$.

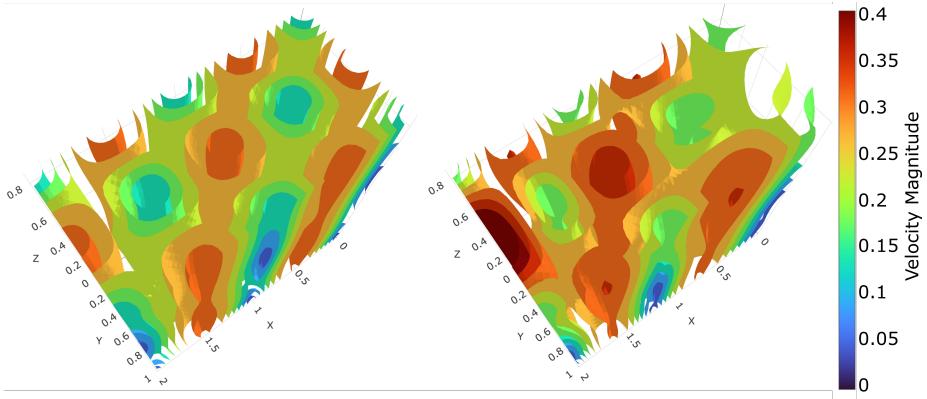

(b) Velocity magnitude isosurfaces for double-gyre flow (1) at $t = 0$ and $t = 3.4$.

Figure 2: 3DSeaVizKit demonstrative (a) cross-section and (b) isosurface visualizations of velocity magnitude for the canonical 3D double-gyre flow described in equation (1).

2a shows intersecting cross-sections to visualize the velocity magnitude for the double-gyre flow. Since all three spatial dimensions are represented in the visualization, the spatial location and orientation of each cross section in relation to the others provide additional visual context for interpreting 3D fields. In addition to being able to place arbitrary cross sections, the interactivity of the tool allows the user to rotate and pan in order to view different perspectives of the full field.

3.1.2. Scalar Isosurfaces

An isosurface is an embedded surface within a volume representing the level set where all scalar values are of the same constant value.

3DSeaVizKit plots a user-specified number of isosurfaces equally-spaced in scalar value in the range between a designated minimum and maximum limit value. The isosurfaces are rendered and colored according to a colormap ranging

over the limit values. Figure 2b shows two isosurface plots rendered by the toolkit to visualize isosurfaces for the velocity magnitude of the double-gyre flow field as it evolves in time. The surfaces clearly show the centers of the gyres as they oscillate in the x-direction. Since the isosurfaces by definition represent level sets of the scalar field, such plots can be leveraged to visualize regions of the domain where the scalar field is above or below a certain threshold.

3.2. Visualizing Vector-valued Data

The dynamics of a fluid are often expressed through its velocity field, necessitating effective visualization of vector-valued data. The 3DSeaVizKit toolkit renders visualizations of vector-valued data through cone plots and streamtube plots.

3.2.1. Cone Plots

Cone plots are the 3D analogue of a quiver plots, which visualize 2D vector fields $\mathbf{v} = [u, v]$ as arrows over the plotting domain, with the length and direction of the arrow representing the magnitude and direction of each vector, respectively. The vector field data is typically input as components, with arrays containing the scalar components u and v of the vector field. Similarly to how quiver plots represent 2D vector fields, a cone plot can be used to visualize a 3D vector field $\mathbf{v} = [u, v, w]$ as distinct cones, with the size of each cone representing the magnitude of the vector and the direction of the cone aligned according to the scalar components u, v, and w. An example cone plot of the velocity field in the Mid-Atlantic region is shown in the flowchart in Figure 1, highlighting the Gulf Stream.

3.2.2. Streamtube Plots

A streamline is a line that is everywhere tangent to the instantaneous velocity field direction. Since at every point in space, the velocity vector has only one direction, streamlines never cross. The tubular region formed by a cross-sectional area of streamlines is a *streamtube*. Streamtubes are useful for visualizing velocity fields because they indicate both the local direction of the flow, as well as the local divergence.

In 3DSeaVizKit, the color of the tube represents the magnitude of the vector at that point, while the diameter of the streamtube represents the deviation from axial flow along each tube at that point in the field as well as the distance from the viewer. In this sense, streamtube plots are useful for examining the instantaneous snapshot of the directional flows of the field.

Figure 3 shows a screenshot of the 3DSeaVizKit GUI used to visualize the double-gyre flow field introduced in §3. Using the GUI, the user can define the starting positions of the streamlines at the center of the tubes. For the example shown in Figure 3, the streamtubes were initialized at the vertical planes $x = 0.5$ and $y = 0.5$, so as to illustrate the helical, circulatory features of the flow.

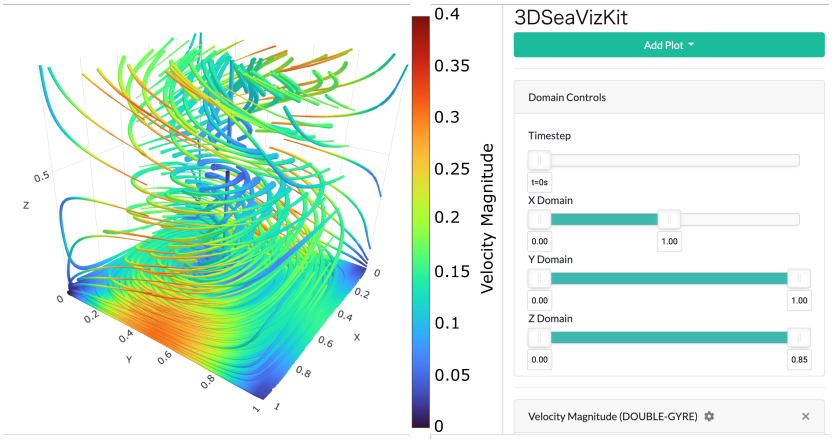

Figure 3: Streamtube visualization of the helical velocity field from the canonical 3D double-gyre flow, interactively visualized on a domain subsection using the 3DSeaVizKit Graphical User Interface.

3.3. Visualizing Trajectory Data

3DSeaVizKit allows for the visualization of trajectory/path line data from drifters or water parcels seeded at initial locations and advected according to the ocean dynamics over time using the forward-Euler or higher-order time marching schemes, visualizing the dynamics in a Lagrangian sense rather than an Eulerian sense. The toolkit allows for filtering trajectories according to a Boolean criteria, such as selecting all trajectories which reach a certain depth or portion of the domain. Additionally, the toolkit allows for coloring each trajectory based on auxiliary data; for example, colormaps over the trajectory data can indicate time or oceanographically relevant quantities such as the velocity magnitude, vorticity magnitude, or fluid density experienced by each parcel along its trajectory.

Figure 4 shows the parcel trajectories in the double-gyre flow field. The trajectories shown provide a Lagrangian perspective of the flow field by depicting the path taken by each parcel over time. In particular, Figure 4 highlights the flow separatrix plane of the double-gyre: most of the parcels that are seeded at $z = 0.5$ to the left of the separatrix plane at $x = 1$ remain trapped in the left gyre, while only a few trajectories cross the separatrix to the right gyre.

3.4. Time-dependent Visualization and Interactivity

The toolkit also provides interactive visualizations over discrete time units for temporally dependent data. The back-end data specification includes a separate time index corresponding to temporally dependent netCDF data, and the front-end GUI contains a slider allowing the user to interactively animate the visualization once the plots have been configured as desired.

Additionally, the GUI allows for on-the-fly customization of plot configuration, with the option to switch out colormaps as well as to change color limits and data minimum and maximum levels. The rendering limits of the domain can

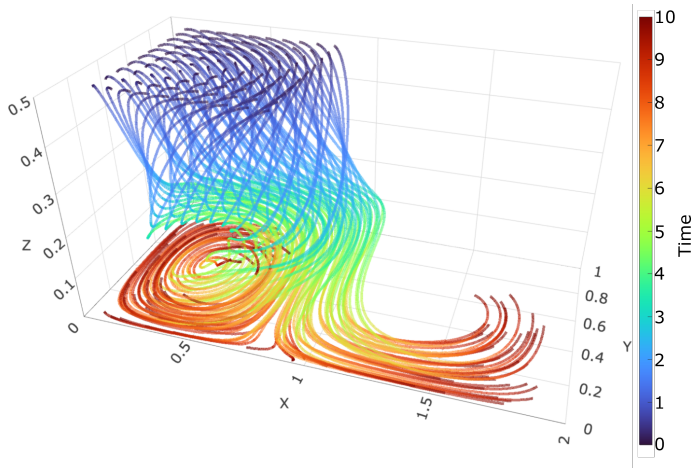

Figure 4: 3DSeaVizKit visualization of parcel trajectories starting at $z = 0.5$ and advected by the 3D double-gyre flow in equation (1) for the duration $t \in [0, 10]$.

also be changed interactively using sliders for latitude range, longitude range, and depth range. The opacity of cross-sectional plots can be adjusted to show multiple plot types at a time, and the xyz-position of the light source can be changed to alter the shading on the bathymetry and rendered surfaces.

4. Applications

This section showcases the application of 3DSeaVizKit to data-assimilative simulations from multidisciplinary ocean modeling research and sea experiments undertaken by the MSEAS group and collaborators. The modeling domains for these research projects and sea experiments are depicted in Figure 5. Table 1 highlights the details of the simulations used in each case. For reference, all visualizations in this paper were generated on a consumer-grade laptop computer.

Table 1: MSEAS sea experiments: Project, location of domains, resolution, and spatial grid size of multiresolution ocean simulations.

Project	Location	Resolution		Grid Size
		Horizontal	Vertical	
NSF-ALPHA	Nantucket & Martha's Vineyard (shelf)	600m	$0.02 - 40$m	$282 \times 337 \times 20$
	Martha's Vineyard	200m	$0.02 - 10$m	$294 \times 323 \times 20$
BIOMAPS	Massachusetts Bay	333m	$0.05 - 5$m	$451 \times 266 \times 100$
GOM	Gulf of Mexico	$1/12.5°$	$0.02 - 380$m	$158 \times 230 \times 100$
CALYPSO	Alboran Sea	$1/200°$	$0.06 - 200$m	$480 \times 773 \times 70$
	Motril Marginal Plateau	$1/600°$	$0.06 - 140$m	$480 \times 773 \times 70$

4.1. NSF-ALPHA: Transport Phenomena Around Nantucket and Martha's Vineyard

We first consider the NSF-ALPHA project which investigated Lagrangian methods for transport processes and completed real-time sea experiments around the islands of Nantucket and Martha's Vineyard near Cape Cod, MA in the United States [63]. In 2018, a real-time at-sea experiment was performed for

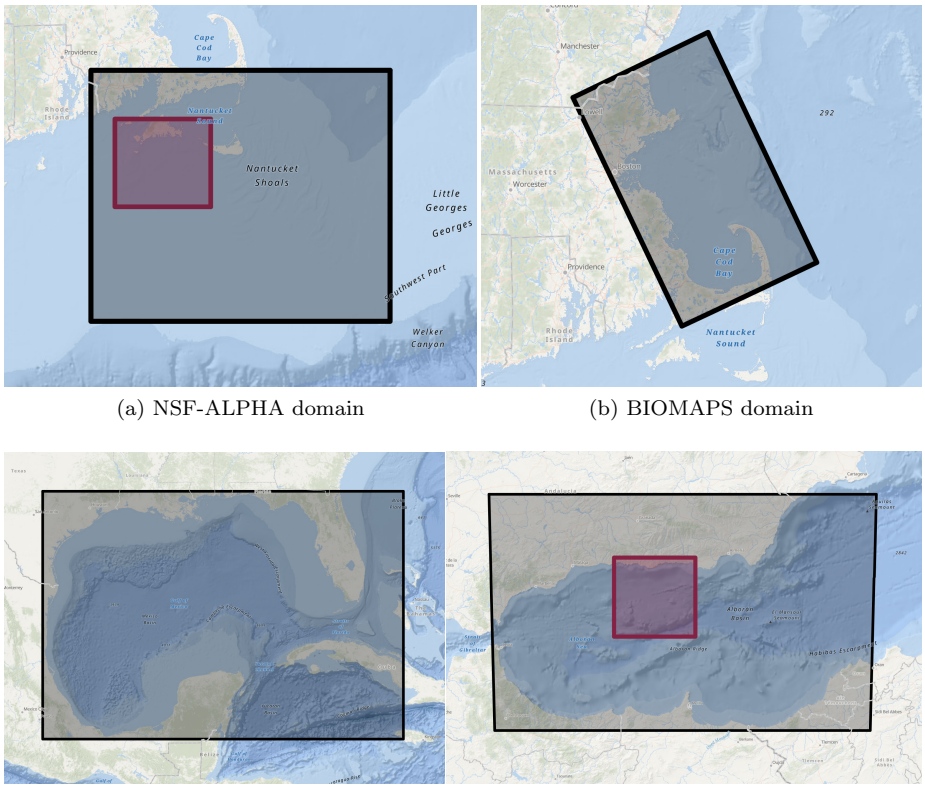

(a) NSF-ALPHA domain (b) BIOMAPS domain

(c) GOM domain (d) CALYPSO domain

Figure 5: Modeling domains of the MSEAS-PE data-assimilative multiresolution probabilistic simulations for the (a) NSF-ALPHA project and 2018 real-time sea experiment in the Nantucket and Martha's Vineyard coastal region with implicit 2-way nested domains [62, 63], (b) BIOMAPS project and simulations around the Massachusetts Bay region [64, 65], (c) GOM project and simulations covering the Gulf of Mexico and surrounding areas of the Atlantic Ocean [66, 67], and (d) CALYPSO project and 2019 real-time sea experiments in the Alboran Sea, the westernmost portion of the Mediterranean [68, 69], with implicit 2-way nested domains. Red regions indicate 2-way nested higher-resolution modeling domains. The elevation data were obtained from the GEBCO_2022 grid [70].

the NSF-ALPHA project during August 1–18. The MSEAS modeling system provided real-time forecasts of temperature, salinity, velocity, sea surface height (SSH), vorticity, 2D and 3D flowmaps, and Finite-time Lyapunov Exponents (FTLEs), all of which were issued several times per day. Special products were also issued including ensemble forecasts, drifter forecasts, other Lagrangian products to aid in drifter recovery, and quantitative adaptive sampling guidance. After the experiment, there was a clear need for robust 3D visualization. We used 3DSeaVizKit interactively to reveal, display and analyze ocean dynamics and coherent structures.

In real-time, the MSEAS modeling system was set up with the implicit

two-way nested domains depicted in Figure 5a. The larger (shelf) modeling domain contained $282 \times 337 \times 20$ finite volumes with a horizontal resolution of 600 m and 20 optimized terrain-following levels with a vertical resolution varying from about 0.02 m to 40 m. The nested sub-domain contained $294 \times 337 \times 20$ finite volumes with a horizontal resolution of 200 m and 20 optimized terrain-following levels with a vertical resolution varying from about 0.02 m to 10 m. The bathymetry was obtained from the United States Geological Survey's 3-arcsecond Gulf of Maine database [71]. The simulations were initialized using synoptic and historical temperature and salinity data from the National Marine Fisheries Service [72] and the World Ocean Database [73], new feature models that build upon [74, 75], and 2017 satellite sea surface temperature [76]. Primitive-equation-balanced velocities were constructed from these mapped T/S fields and optimized for our high-resolution coastlines and bathymetry [39, 77, 78]. Atmospheric forcing was obtained from the NAM Forecast System [79]. Tidal forcing from the TPXO8-Atlas [80, 81] was adjusted to our higher-resolution bathymetry and quadratic bottom drag.

Figure 6 depicts 3DSeaVizKit visualizations of the MSEAS-PE real-time forecast of the August 17, 2018, temperature and relative vorticity fields over the 600 m-resolution shelf numerical modeling domain (Fig. 5a). From the 3D temperature visualization (Fig. 6a), we clearly observe the colder waters on Nantucket Shoals (southeast of Nantucket island) with relatively uniform (cold) temperatures at each of these depths. This well-mixed zone is due to strong tidal-induced mixing [82]. The striations in vorticity over the Nantucket Shoals (Fig. 6b) indicate that the mixing is associated with vertical cells and tidal residual eddies and jets, in part due to the interactions with the northeast-trending ridges of the seabed bathymetry. Frequently, some of these waters on the shoals are transported westward along isobaths or to the deeper regions, by tidal residual currents, coastal currents, and overflows on top of offshore waters. The 3D visualization for August 17, 2018, allows us to plainly see this offshore westward transport in the temperature field (Fig. 6a) and in the associated high and low lines of vorticity on the sides of the currents (Fig. 6b). Figures 6c and 6d are the result of interactive zooms on the New England Shelfbreak Front region on the southern side of the shelf domain. The zooms highlight the train of surface submesoscale eddies and regions of high vorticity that result from the meanders and eddy-shedding along the tilted shelf break front [42]. The front separates the waters of the shallow shelf from those of the slope and deeper Atlantic Ocean. This is another region of very high vorticity and nonlinear dynamics. The surface-intensified eddies are created after the high-shear front enters the domain and remain tilted along the front down to 39 m and deeper.

Figure 7 still illustrates MSEAS-PE real-time forecast fields again for August 17, 2018, but now over the 200 m-resolution Martha's Vineyard domain, implicitly 2-way nested within the shelf domain (Fig. 6). The 3D temperature and vorticity visualizations in the high-resolution nested domain (Figs. 7a–7b) clearly highlight the westward overflows from the Nantucket shoals and the Nantucket–Martha's Vineyard coastal current [62]. At depth, the coastal current is associated with vorticity striations and internal vertical motions confirmed by

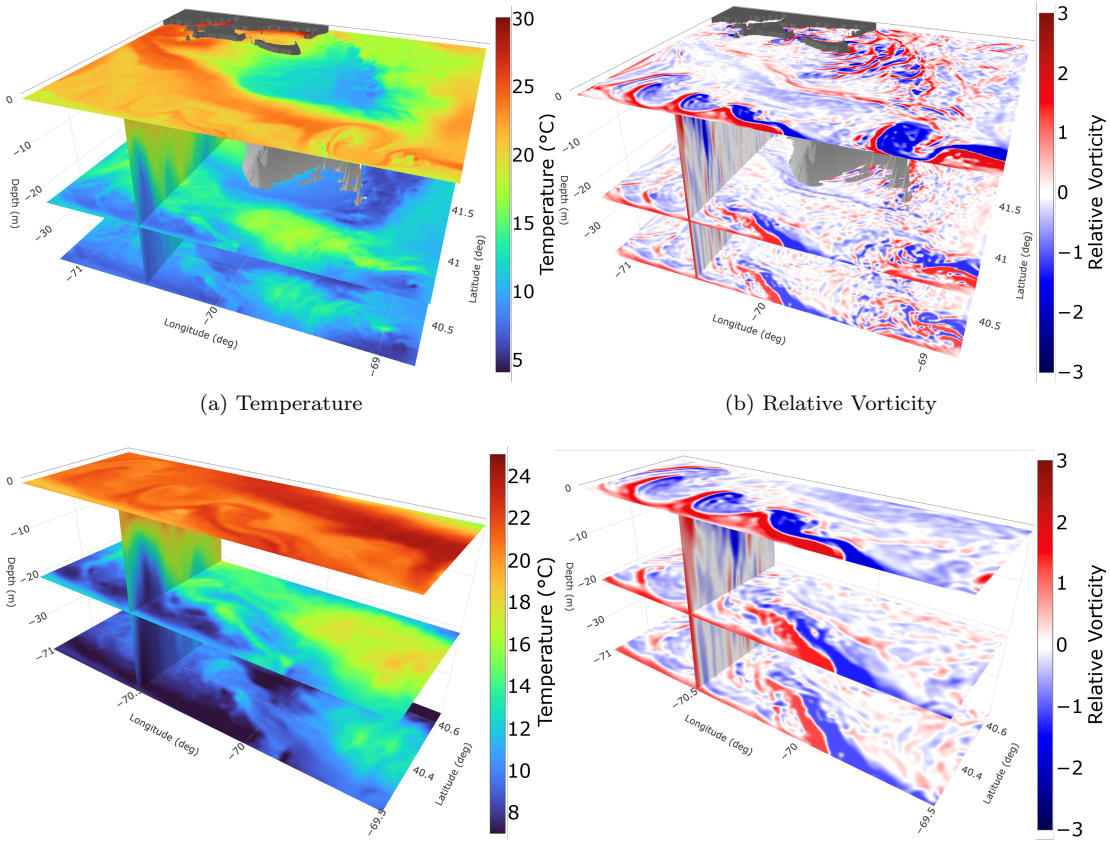

(a) Temperature

(b) Relative Vorticity

(c) Temperature Zoom, New England Shelfbreak Front

(d) Relative Vorticity Zoom, New England Shelfbreak Front

Figure 6: NSF-ALPHA shelf domain: 3DSeaVizKit temperature (°C) and relative vorticity (ω/f, non-dimensional) visualizations. The real-time MSEAS-PE fields correspond to the implicit 2-way nested forecast for 18:00 UTC, August 17, 2018, and are shown at depths of 1 m, 21 m, and 39 m, along with a cross-section at 70.5°W, visible to the south of Martha's Vineyard. (a–b) Temperature and vorticity fields in the whole domain. (c–d) Zoom on the New England Shelfbreak Front, with a cooler colorbar for temperature.

submesoscale temperature wave bands mostly parallel to the front as well as by responses due to bathymetric variability. Tidal fronts are also visible south of Muskeget Channel (channel separating Martha's Vineyard and Nantucket) and west of Nomans Land (the small island southwest of Martha's Vineyard) at the mouth of Buzzards Bay. The corresponding internal waves lead to cooler and warmer curved bands in the surface temperature and to negative and positive curved bands in surface vorticity. Often, they lead to submesoscale tidal residual eddies that are advected by the flow. The zooms (Figs. 7c–7d) highlight all these tidal features just south of Muskeget Channel. Internal waves and complex motions are observed across and south of the Channel, with a very

shallow summer diurnal warm layer (Fig. 7c) and baroclinic mode motions in the vertical (Fig. 7d).

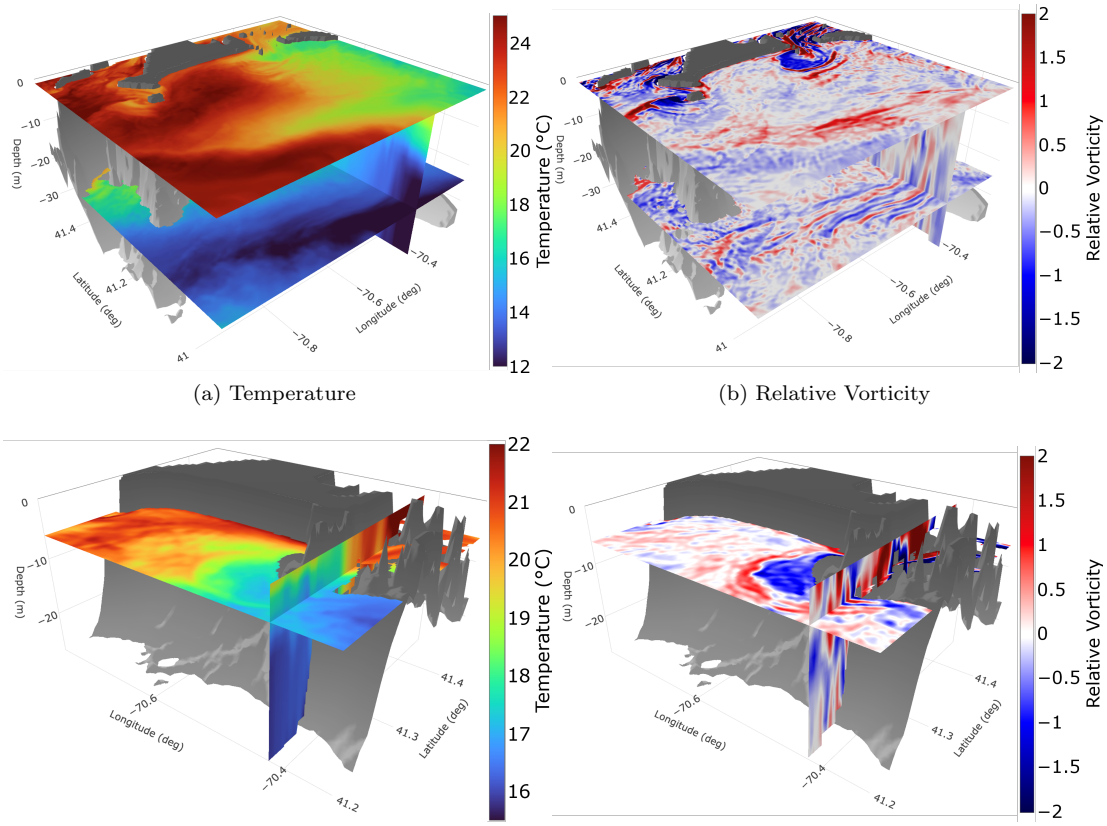

(a) Temperature

(b) Relative Vorticity

(c) Temperature Zoom, Muskeget Channel Outflow

(d) Relative Vorticity Zoom, Muskeget Channel Outflow

Figure 7: NSF-ALPHA implicit 2-way nested Martha's Vineyard domain: 3DSeaVizKit temperature (°C) and relative vorticity (ω/f, non-dimensional) visualizations. The real-time MSEAS-PE fields correspond to the implicit 2-way nested forecast for 18:00 UTC, August 17, 2018. (a–b) Temperature and vorticity fields at depths of 1 m and 25 m, along with a cross-section through Muskeget Channel (70.425°W). (c–d) Temperature and vorticity fields at 5 m depth, along with an outcroping cross-section through Muskeget Channel (70.425°W). Note the temperature colorbars differ and when compared to Fig. 6 the relative vorticity colorbar was reduced to $[-2, 2]$ to highlight features south of the channel.

We also employed 3DSeaVizKit to render Finite-time Lyapunov Exponent (FTLE) fields, a dynamical quantity commonly used to identify Lagrangian Coherent Structures (LCSs) in the flow [57, 83, 84, 50, 85]. Once velocity fields were forecast, we used our PDE-based method of composition for open ocean domains [51, 86] to forecast Lagrangian flow maps and FTLE ridges. Flow maps are dynamic spatiotemporal fields that correspond to an infinite number of classical trajectories: they provide the positions of purely advected water

parcels, either forward or backward in time [87]. FTLE fields are a logarithmic rescaling of the largest singular value of the gradients of these flow maps [85, 62]. Forward- and backward-time FTLE fields were computed and visualized; their ridges approximate the repelling and attracting Lagrangian flow structures [83], respectively.

For example, to quantitatively describe transport features in the Muskeget Channel, we employed the MSEAS-PE forecasts in the 2-way nested Martha's Vineyard domain at 200 m resolution and predicted FTLE fields in real-time [63]. We used these FTLE fields to delineate attracting and repelling flow structures and to design and complete search and rescue experiments [2]. Figure 8 shows the 36-hour duration backward FTLE field, from 20:00 UTC on August 17 to 08:00 UTC on August 19, 2018, as computed in real-time at 200 m resolution. The ridges of this FTLE field approximate the attracting manifolds over the time window of interest; these more persistent structures tend to attract water parcels. From the FTLE field, the coherent structures in the flow can be clearly observed at the surface, and particularly inside and immediately southwest of Muskeget Channel, which indicates a flow convergence zone over the 36 hours of interest. Such convergence in the flow is due to the effect of tides and topography around the channel. These ridges are not as well defined at a depth of 30 m, indicating that, while there is vertical mixing, the Lagrangian transport of water through the channel occurs mainly in the surface layers. This is in accord with the baroclinic properties shown in Fig. 7.

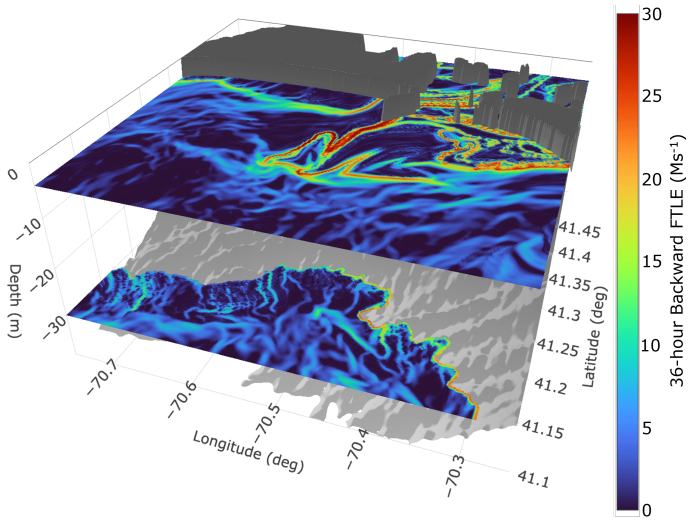

Figure 8: NSF-ALPHA Martha's Vineyard domain: 3DSeaVizKit visualization of the MSEAS-PE 36-hour integrated backward FTLE field, forecast for the duration 20:00 UTC on Aug. 17 to 08:00 UTC on Aug. 19, 2018, in the 2-way nested domain at 200 m resolution. The depth sections shown are located at 4 m and 30 m. (Units are inverse megaseconds: 1 Ms^{-1} = 10^{-6} s^{-1})

When ocean quantities vary significantly in space, the above utilization of multiple horizontal maps and cross-sections helps visualizing the 3D variation of

each field including bathymetric effects. It provides the oceanographer a visual sense of the full 3D fields. Structural details varying across depths and horizontal locations are revealed, even when they are not easily discoverable in separate 2D plots alone. Since the toolkit allows for the placement of arbitrarily many maps and cross-sections at arbitrary locations as well as interactive panning and zooming, the 3DSeaVizKit interactive visualizations of scalar fields provide tremendous exploratory potential for making sense of ocean simulation data.

4.2. BIOMAPS: Biogeochemical Fields in Massachusetts Bay

Predicting and monitoring the health of marine ecosystems is essential for the protection and utilization of our oceans and life on Earth [88, 89]. Ocean acidification, the decrease in seawater pH over time, is one of the climate change processes that can severely impact pristine marine ecosystems and key coastal industries [90, 91]. For example, it is directly relevant in Massachusetts Bay for shellfish aquaculture [92]. For this second application of 3DSeaVizKit, we consider our BIOMAPS research and ocean acidification modeling in the Massachusetts Bay region [64, 65].

To predict and monitor ocean acidification, models and observations of biogeochemical fields such as nitrate (NO_3), ammonium (NH_4), zooplankton (Z), detritus (D), chlorophyll (Chl), dissolved inorganic carbon (DIC), total alkalinity (TA), and calcium carbonate ($CaCO_3$) concentrations are needed. A coupled physical-biogeochemical-acidification hindcast of Massachusetts Bay during 11 August–13 September 2019 was made using the MSEAS-PE modeling system. The modeling domain (figure 5b) contained $451 \times 266 \times 100$ finite volumes with a horizontal resolution of 333 m and 100 optimized terrain-following levels with a vertical resolution varying from about 0.05 m to 5 m. The bathymetry was obtained from the USGS 3-arcsecond Gulf of Maine database [71]. For the physical fields, the subtidal initial and boundary conditions were downscaled from 1/12° HYbrid Coordinate Ocean Model (HYCOM) analyses [93] via optimization for our higher resolution coastlines and bathymetry [39]. Local corrections were made using synoptic CTDs of opportunity and a feature model for the Maine Coastal Current [75]. Tidal forcing was reprocessed from the high resolution TPXO8-Atlas for our higher resolution bathymetry/coastline and quadratic bottom drag (a nonlinear extension of [40]). The atmospheric forcing consisted of hourly analyses/forecasts of wind stress, net heat flux, and surface freshwater flux from the 3 km NAM [79]. For the coupled biogeochemical fields, we employ our generalized biogeochemical model [94]. It was configured as a 7-component system: NO_3, NH_4, Chl, Z, D and two phytoplankton (P) components tracking NO_3 and NH_4 uptake. The biological fields and parameters were initialized using in situ and historical data and tuned to August–September conditions, starting from the parameters in [47]. Historical data for NO_3 and Chl were obtained from the World Ocean DataBase [73] and objectively analyzed to produce 3D fields for August and September. To ensure balanced and consistent initial and parameter conditions, the fields that were not observed or only partially observed (NH_4, Z, D, P) were dynamically adjusted using our biogeochemical

equations in a weak constraint form [77, 78, 47]. We then added an ocean acidification model based on [95], adapted to our particular physical-biogeochemical system. The model predicts DIC, TA, and $CaCO_3$, with the remaining acidification fields obtained from the equilibrium model CO2SYS [96]. DIC and TA were initialized by empirical models [DIC(σ_θ) and TA(S)] created specifically for the Gulf of Maine using historical WODB and Gulf of Mexico and East Coast Carbon Cruise data [GOMECC; 97, 98]. $CaCO_3$ was initialized as an unobserved variable via dynamical adjustment of our acidification equations in a weak constraint form.

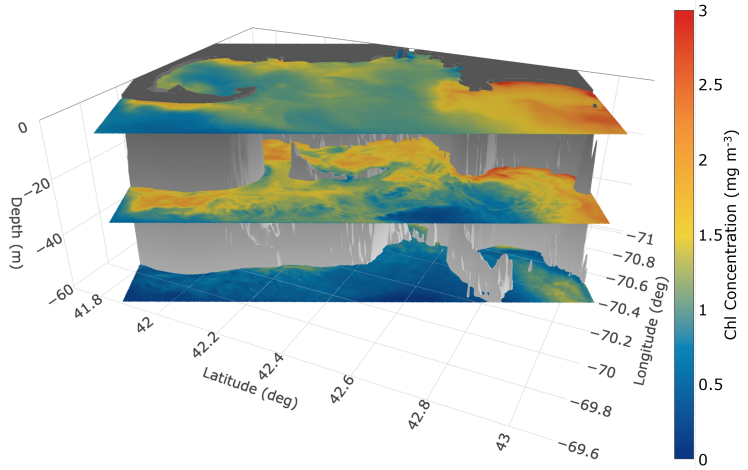

Figure 9: BIOMAPS: 3DSeaVizKit visualization of MSEAS physical-biogeochemical simulation of chlorophyll concentration ($\mathrm{mg\,m^{-3}}$) in Massachusetts Bay. The chlorophyll fields shown correspond to a hindcast for 12:00 UTC, Sep. 5, 2019, and are displayed at depths of 1 m, 31 m, and 61 m.

4.2.1. Visualization of Biogeochemical Processes

Figure 9 shows a 3DSeaVizKit visualization of the data-assimilative MSEAS coupled physical-biogeochemical simulation of chlorophyll concentration in Massachusetts Bay. The chlorophyll fields are shown at depths of 1 m, 31 m, and 61 m at 12:00 UTC, September 5, 2019. The 3D visualization, along the coasts at the surface and mid-depth, reveals enhanced concentrations of chlorophyll fed by nutrients brought up from depth by wind-induced upwelling [99, 47]. At the surface on that day, the chlorophyll has largely used up the nutrients and been depleted by zooplankton. It is higher at the inflow from the north along the Maine Coastal Current and, to a lesser extent, just offshore of the inner coastline of the Bay due to recent upwelling. At mid-depth (31m), the chlorophyll has access to both increased nutrients pumped up from deeper regions and sufficient sunlight to create sub-surface maxima. On that day, the chlorophyll is higher around Stellwagen Bank, partly in response to internal tides generated at the Bank. Deeper still (61m), the reduced light levels inhibit the growth of chlorophyll. South of Cape Ann (near 42.6°N, 70.6°W), we see a double maxi-

mum (near surface and at mid-depth) created by a combination of wind-induced upwelling, internal tides, and the advection of near-surface fields [64].

4.2.2. Visualization of Ocean Acidification

The 3DSeaVizKit visualization of the MSEAS simulated pH for Massachusetts Bay is presented in Figure 10. The pH fields are shown at the same depths as chlorophyll, 1 m, 31 m, and 61 m, and same time, 12:00 UTC, September 5, 2019. Overall, the 3D pH visualization reveals a mid-depth maximum and lower pH values near the surface and at depth. The decrease in pH with depth is consistent with the initial conditions estimated from a combination of empirical and equilibrium models [64]. In contrast, a combination of physical and biological dynamics caused the decrease of pH at the surface during the simulation (not shown). In particular, our 3D visualization enables linking the more acidic surface waters (lowest surface pH) to locations where the surface chlorophyll is depleted (in Cape Cod Bay, off shore of Cape Cod, in Boston Harbor around 42.3°N, 70.9°W, and near Salem Harbor around 42.5°N, 70.9°W). The effects of internal tides can be seen by the filament of lower pH water east of Stellwagen Bank (around 42.2°N, 70.2°W) in which the internal tides propagating off Stellwagen Bank have mixed lower pH water from the surface down to mid-depth. Finally, more acidic (lower pH) waters are being advected from the Gulf of Maine along and through the eastern boundary (e.g., near 42.6°N, 70.1°W). This lower pH water from the Gulf of Maine is consistent with the observation of the acidification of the deeper waters in Wilkinson Basin [100].

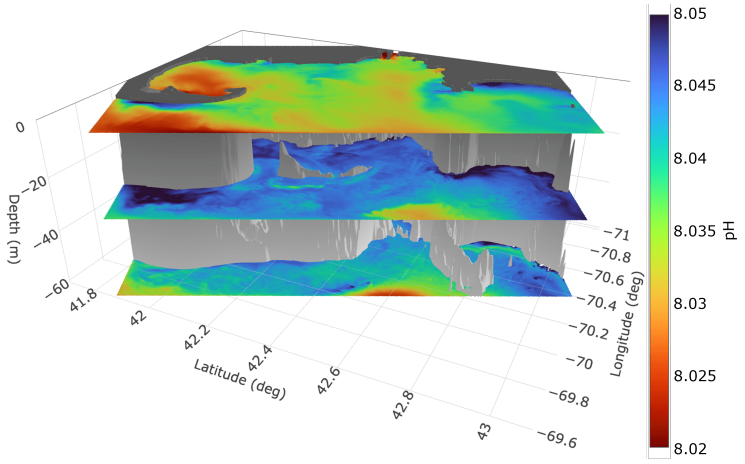

Figure 10: BIOMAPS: 3DSeaVizKit visualization of MSEAS simulated pH field in Massachusetts Bay. The pH fields shown correspond to a hindcast for 12:00 UTC, Sep. 5, 2019, and are displayed at depths of 1 m, 31 m, and 61 m. Note that the colormap is flipped, i.e. red corresponds to the smaller pH (more acidic) values, and blue corresponds to the larger pH (less acidic) values, to conform with the pH universal indicator convention.

4.3. GOM: Gulf of Mexico Loop Current System

The 3DSeaVizKit vector field visualization capabilities were used in the context of a multi-institution collaborative project to achieve a better understanding of the physical processes that control the circulation in the Gulf of Mexico (GOM), in particular, the Loop Current (LC) and Loop Current Eddy (LCE) separation dynamics [101, 102, 103, 67, 104, 105, 106]. For the present work, the geographic MSEAS-PE modeling domain considered is depicted in Figure 5c [66]. This domain has a horizontal resolution of 1/12.5° (about 9 km), using a finite-volume grid of size $158 \times 230 \times 100$ with 100 terrain-following levels possessing a vertical resolution varying between 0.02 m and 380 m for the deepest GOM zones. The model is forced with tides from TPXO8-Atlas data from OSU, adapted to the high-resolution bathymetry and coastlines, and is atmospherically forced with hourly 1/5° NCEP CFS output [107]. The sub-tidal initial and boundary conditions are downscaled from HYCOM [93, 108], with optimized velocities for high-resolution coasts and bathymetry [39]. The hindcasts cover the period from May 24 to June 28, 2015.

The 3DSeaVizKit streamtube visualizations of the Loop Current system in the GoM are illustrated in Figure 11. Such colored streamlines with variable thickness are useful to depict the location of currents and eddies, and the variability in their circulation strength in 3D as the width of the streamtubes is related to the depth of field and flow properties, in addition to the colored local magnitude of the velocity field. For both visualizations, Figs. 11a–11b, the starting positions of the streamtubes are defined from the vertical planes located at 24.8°N and 86.65°W. This 3D visualization showcases the main Loop Current 3D structures and related LCEs; we observe the LC entering the Gulf through the Yucatan Channel between Mexico and Cuba and exiting through the Florida Strait between the Florida Keys and Cuba, with 3D currents decaying with depth. On May 26, the strongest currents occur on the western side of the main LC, along the eastern escarpment of Campeche Bank, and west of Florida, especially just west of the Bahamas. However, by June 6, the strongest currents have weakened along the interior LC with multiple LCEs, but strong currents still occur west of Florida. Throughout the period May 26 to June 6, 2015, the current is in an extended state, but undergoing a state transition [109], with the eddy *Nautilus* (center located at approximately 26°N, 90°W throughout the period) reattaching to the main current. The streamtubes enable tracking *Nautilus* as it begins to split into the two sub-eddies *Nautilus I* and *Nautilus II*, the latter of which is located at approximately 24.5°N, 92°W on May 26 (Figure 11a). Eddy *Nautilus II* slowly drifts westward and has fully detached from *Nautilus I* by June 6 (Figure 11b). Farther west, remnants of the dissipating eddy *Lazarus* are visible near the Mexican coast. The still-active eddy *Michael*, centered at approximately 25.5°N, 94.5°W on May 26 (Figure 11a), drifts northwestward toward the Texas coast, arriving there by June 6 (Figure 11b). Finally, eddy *Olympus* begins to form inside the northwest extent of the main Loop Current, a process that continues throughout June; this eddy separates from the main current by the end of the month. Overall, the 3D

streamtube visualization clearly highlights these spatial and temporal variabilities of the LC system.

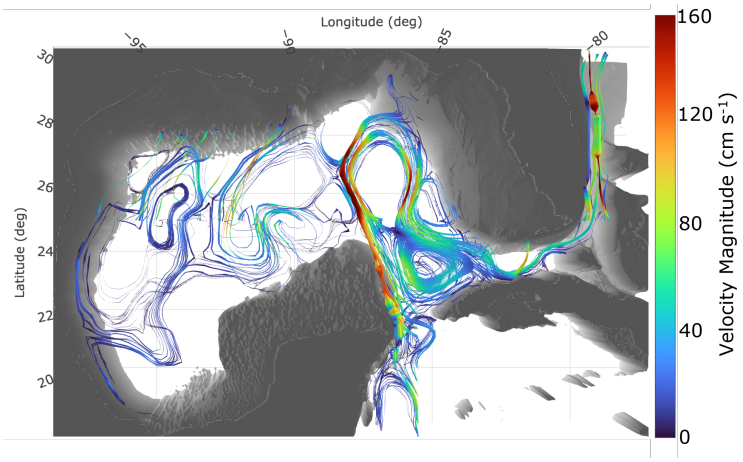

(a) 00:00 UTC, May 26, 2015

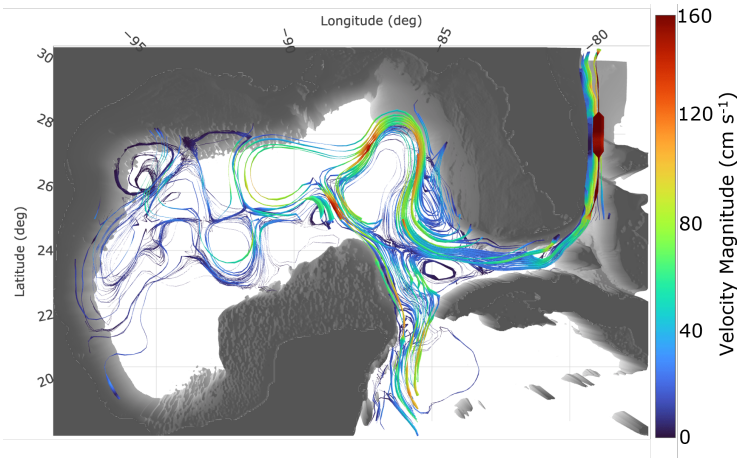

(b) 12:00 UTC, June 6, 2015

Figure 11: GOM: 3DSeaVizKit visualization of 3D streamtubes in MSEAS-PE simulations of the Gulf of Mexico Loop Current System at (a) 00:00 UTC, May 26, 2015, and (b) 12:00 UTC, June 6, 2015. The starting positions of the streamtubes were defined from two vertical seeding planes, each a 15×10 grid with 10 evenly spaced depths spanning [0 m, 1000 m]. The first is along 24.8°N and has 15 evenly spaced points spanning [97.882°W, 77.989°W]. The second is along 86.65°W and also has 15 evenly spaced points spanning [18.133°N, 30.467°N]. The streamtubes are colored by the magnitude of the local velocity ($\mathrm{cm\,s^{-1}}$) and their thickness decreases with depth.

Next, we use 3DSeaVizKit to investigate the 3D relative vorticity fields, shown in Fig. 12. In addition to highlighting the structures traced by the streamtubes, the vorticity maps reveal additional features and details in regions that the shown streamtubes did not visit, with the 3D visualization again revealing

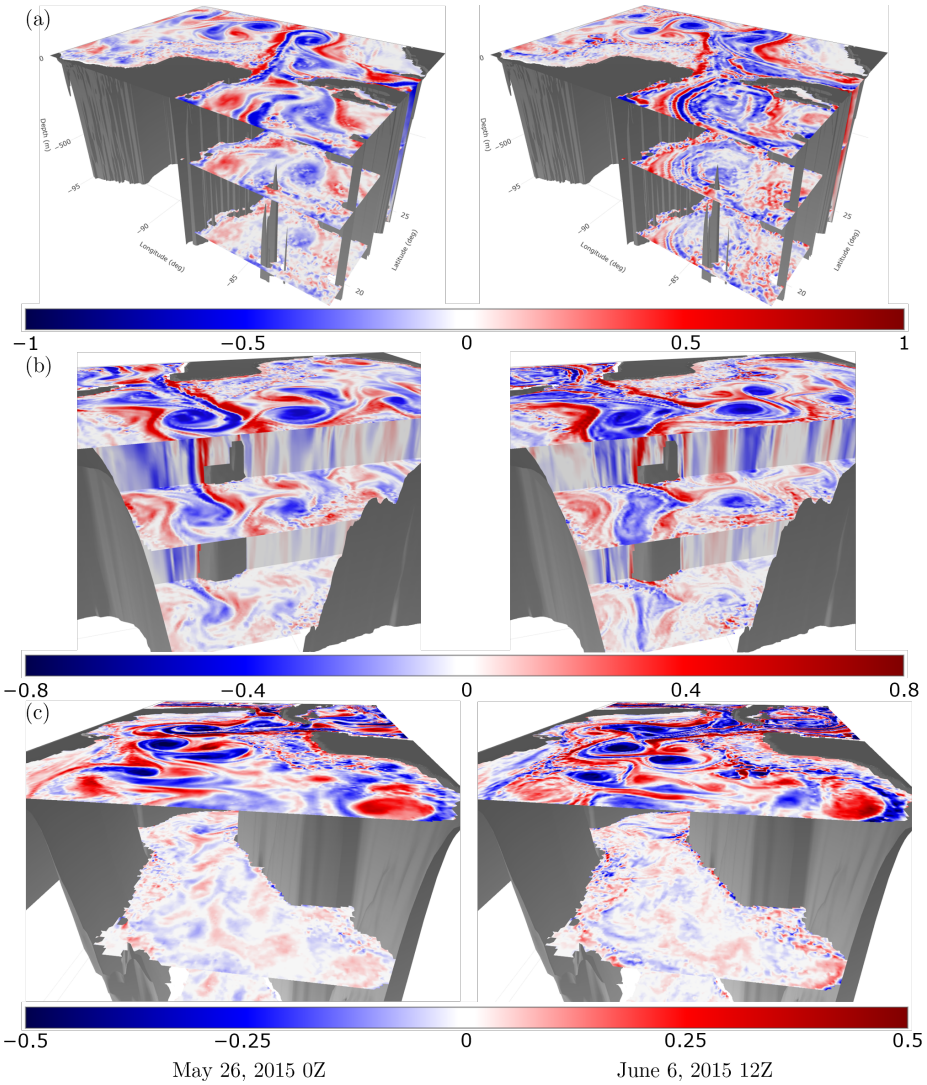

Figure 12: GOM: 3DSeaVizKit visualization of MSEAS-PE relative vorticity (ω/f, nondimensional) in the Gulf of Mexico at 0Z on May 26, 2015 (left column) and 12Z on June 6, 2015 (right column). (a) View from the southeast (i.e., from the Caribbean Sea); the relative vorticity is shown at 1, 301, and 701 m depth and in a vertical section along 24°N. (b) View from the northeast (i.e., from the US Gulf Coast); the slices shown are the same as the top row. (c) View from the west; the relative vorticity is shown at 1, 1001, and 2001 m depth. Note that colorbar limits differ.

otherwise hidden structural details across space. Fig. 12a shows the northward inflow from the Caribbean Sea, including a large anticyclonic gyre or eddy that is most intense at the surface but spans the upper 700 m. This Caribbean feature is present on May 26, advects westward, and strengthens through June 6, while smaller-scale streamers and filaments also develop during this period. Strong

flow through the Florida Strait is likewise visible. Fig. 12b presents the vertical structure of the LC and LCEs, viewed from the northeast, illustrating how the 3D visualization helps connect horizontal surface patterns with their vertical structure. On May 26, most vorticity structures extend throughout the entire upper 700 m, as demonstrated by the vertical section along 24°N, which passes through the center of eddy *Nautilus II*. The 3D visualization also highlights two notable exceptions: a small cyclonic recirculation eddy, approximately 100 km in diameter, that forms between the inflow and outflow branches of the LC and is confined to the upper 300 m, and a northward-flowing streamer in the western GOM near 95°W that feeds into LCE *Michael*. At 24°N the anticyclonic vorticity of this streamer is also limited to the upper 300 m, although it extends deeper farther north. At this time, the eastern GOM exhibits stronger vorticity than the western basin. By June 6, however, the vorticity in the western GOM strengthens, and only smaller-scale, topographically driven vorticity structures fail to encompass the upper 700 m. Fig. 12b also emphasizes that the LC extends farther to the northeast over this period than is evident in Fig. 11. Fig. 12c further reveals the deeper vertical structure—down to 2000 m—in the western GOM, viewed from the west. On May 26 a strong signature of the LC appears at 1000 m and intensifies through June 6, while weaker signatures of LCEs *Nautilus I* and *Nautilus II* are also visible at this depth on both dates. In contrast, the older LCE *Michael* shows no obvious signature at 1000 m. Leveraging 3DSeaVizKit enables us to explicitly highlight that in the western GOM the correlation between vorticity at 0 m and 1000 m is weaker than in the LC and LCEs, and the correspondence decreases further between 1000 m and 2000 m. In general, the 3D visualization indicates that the LC and younger LCEs are largely confined to depths above 2000 m but retain a significant presence at 1000 m, whereas older LCEs can become more vertically attenuated through accumulated shear, mixing at LCE edges, and topographic interactions. Smaller-scale features, such as Loop Current Frontal Eddies (LCFEs) [110, 106] and topographically generated vorticity, exhibit an even more limited vertical footprint.

4.4. CALYPSO: Subduction Regions in the Alboran Sea

The CALYPSO collaborative initiative addresses the challenge of quantifying the three-dimensional, time-dependent transports of ocean properties from the surface ocean to the interior [111, 112, 113, 114]. A central goal is to predict and characterize multiscale ocean transports and subduction processes, that is, the downward transport of surface quantities. The first focus was the Alboran Sea region in the western Mediterranean Sea, and the MSEAS-PE ocean modeling system was set up in the domain depicted in Figure 5d [69, 115, 116, 68]. The horizontal resolution of the Alboran Sea domain used in the simulations was $1/200^\circ$ (about 500 m) within a 480×773 horizontal grid with 70 vertical terrain-following levels providing a vertical resolution between 0.06 m and 200 m. The nested Motril Marginal Plateau domain had a horizontal resolution of $1/600^\circ$ (167 m), also within a 480×773 horizontal grid, and again with 70 terrain-following vertical levels (resolution between 0.06 m and 140 m). The bathymetry was obtained from the Shuttle Radar Topography Mission (SRTM) 15-arcsecond

global map [117, 118, 119]. For this region, our forecasts span the period from March 20 to April 16, 2019. They were initialized from WMOP [120, 121], and downscaled to our higher resolution domain, using our optimizations for higher resolution coastlines and bathymetry [39, and updates] as well as corrections from real-time data of opportunity. The tidal boundary fields were computed from TPXO8-atlas with adjustments to our higher resolution bathymetry and quadratic bottom drag. The atmospheric forcing was derived from NCEP GFS 1/4° output [122].

Here, visualizations obtained from 3DSeaVizKit were instrumental in unveiling the 3D transport dynamics in the MSEAS real-time forecasts of ocean circulation, subduction events, and uncertainties in the Alboran Sea during March and April 2019; these visualizations and dynamics are discussed next.

4.4.1. Visualization of Gyres and Eddies

Figure 13 shows streamtube plots for the 3D velocity field in the Alboran Sea as forecast for 15:00 UTC, March 26, 2019. The streamtubes' varying velocity magnitudes highlight the complex flow patterns and the dynamic nature of the ocean currents in this region. We also demonstrate how different horizontal and vertical seeding planes (used for the starting positions of the streamtubes), as well as different viewing angles, highlight the 3D structure of the gyres, eddies, and other circulation features. The forecast large, anticyclonic Western Alboran Gyre (WAG) is clearly visible, covering nearly all of the West Alboran Basin (Fig. 13b,d). The velocity varied spatially between 15 to 70 cm/s, with the largest velocities occurring on the eastern and western sides of the WAG. On the east, the WAG pushed up against westward-flowing saline water from the Eastern Mediterranean (Fig. 13c, salinity not shown). This interaction constricted the flow on the east side of the WAG, leading to higher velocities on that side. A second constriction was forecast to occur on the western side of the WAG. This western constriction is caused by a cyclonic recirculation eddy between the WAG and the Moroccan coast (Fig. 13a). East of the Alboran Ridge (36°N, 3°W), a weaker, elongated cyclonic structure centered approximately at 36°N, 2.5°W is forecast (Fig. 13c). This cyclonic structure extended over about 100 km from about 3°W to 2°W with velocity varying between 5 to 15 cm/s. We note that the anticylonic Eastern Alboran Gyre (EAG) was not yet present during this period. By mid-April 2019, the EAG and the Almería–Oran density front develop in the region previously occupied by the cyclonic structure [111].

We compared all of these forecast features with data not available in real-time or held back from the forecast [68]. The AVISO reanalysis (not shown) has a reasonably good agreement with our WAG and the anticyclonic eddy southeast of Cape Sacratif (next paragraph). The AVISO reanalysis also shows some cyclonic structure in the east. We also found that all these forecast features compared reasonably well with the unassimilated *in situ* data (gliders, mooring, not shown). The surface drifters deployed in the experiment were also overall consistent with the larger, longer-lived features (WAG, eastern cyclonic structure).

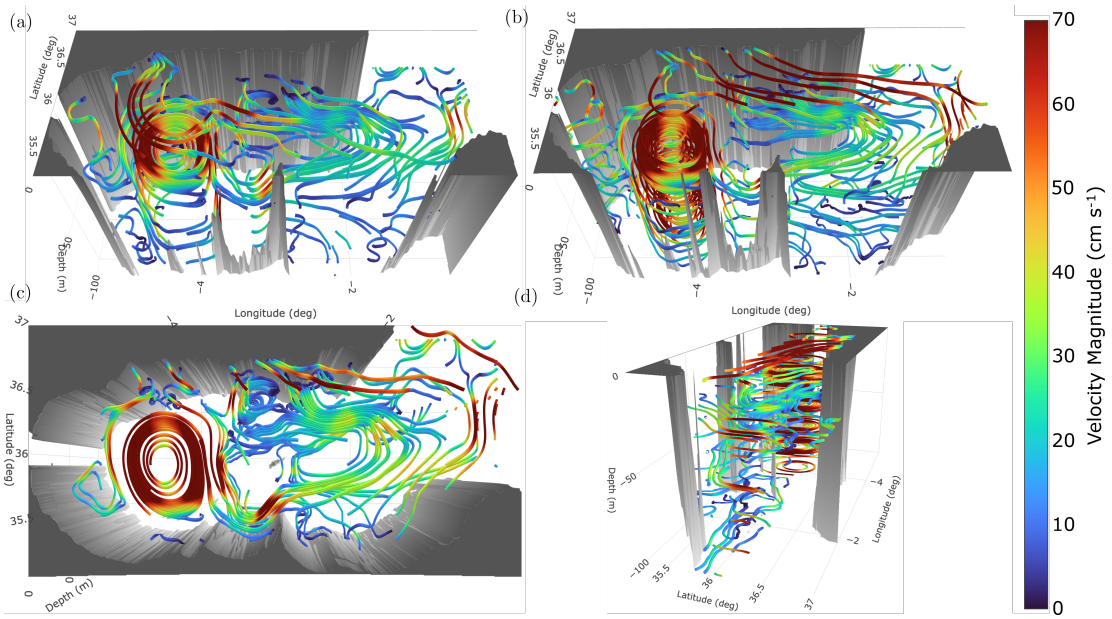

Figure 13: CALYPSO: 3DSeaVizKit three-dimensional streamtube visualizations of the MSEAS-PE reanalysis in the Alboran Sea for the velocity field at 15:00Z on March 26, 2019. It shows the 0-100 m vertical extent of the (a) cyclone by Morocco, (b) anticyclonic West Alboran Gyre, and (c) anticyclone by Cabo Sacratif. It also shows the (d) inflows/outflows of the Alboran Sea with the rest of western Mediterranean Sea, including distinct downwelling as the flow pass the coast of Algeria. Seeding planes and viewing angles were selected to highlight these features. Each panel has two seeding planes used for the starting positions of the streamtubes. All seed the same horizontal plane at 26 m (10×10 grid) with evenly spaced longitudes in [5.3847°W , 0.7113°W] and latitudes in [35.0562°N , 36.9882°N]. We also seed streamtubes in the vertical in a 10×7 plane using the same longitudes and 7 evenly space depths spanning [2 m , 98 m]. These vertical seeding planes are located at 35.5°N (a); 36.0°N (b,d); and 36.5°N (c). The streamtubes are colored by the magnitude of the local velocity ($\mathrm{cm\,s^{-1}}$).

Figure 13 also shows a number of smaller 3D features that were forecast for March 26. The low viewing angle of Fig. 13d highlights a region of subduction as the flow at 26 m goes eastward past the Algerian coast. The O(10 m) drop in the streamtubes is consistent with the ≈ 40 m/day downward vertical velocity seen in the simulation in that region (not shown). The 3D streamtubes of Fig. 13d showcase another downwelling event in that region around the 60 m depth. The 3D visualization also reveals an anticyclonic eddy (36.6°N 3.2°W) to the southeast of Cape Sacratif (Fig. 13c). This particular eddy has a width of about 60 km and was skewed to the west (i.e., the rotational center of the eddy was to the east of the geographic center). The eddy started out fairly gentle, with velocities in the range of 5 to 15 cm/s. It later strengthened due to subsequent wind events (not shown), including a gale blowing to the west on March 26-27, followed by a longer, but weaker wind event on March 28-30 that generally blew to the west but also curled to the northwest around Cape Sacratif.

By March 28-30, the strengthened eddy (not shown) had surface velocities in the range of 20 to 60 cm/s, was transported slightly to the northeast (36.7°N 3.125°W), and entrained a coastal flow past Cape Sacratif. The subduction in and around this eddy is explored with 3DSeaVizKit next.

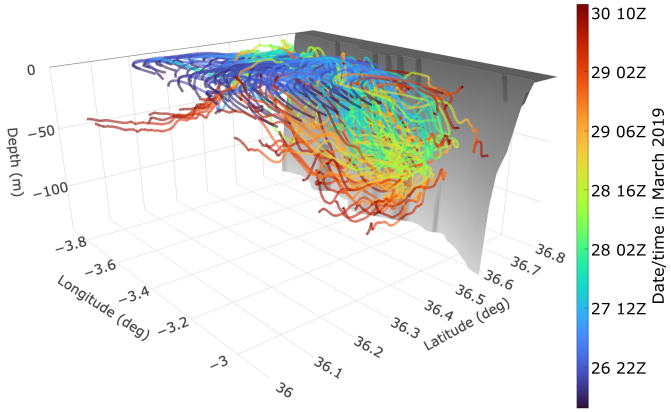

Figure 14: CALYPSO: 3DSeaVizKit visualization of 100 simulated parcel trajectories seeded in the surface waters within a grid between 36.125°N and 36.375°N, and 3°W and 3.75°W. The trajectories are colored with the elapsed time, all starting at 12:00 UTC, March 26, 2019, and with an end time of 12:00 UTC, March 30, 2019. The velocities employed to integrate the trajectories are those of the MSEAS-PE reanalysis.

4.4.2. Visualization of Subduction Dynamics

The trajectory capabilities of 3DSeaVizKit enable users to capture regional subduction dynamics. Figure 14 shows 100 MSEAS-simulated trajectories of parcels seeded on the surface level (finite-volumes in the top 1 to 2 m depths) on a grid between 36.125°N and 36.375°N, and between 3°W and 3.75°W. Initially, the seeded parcels form a grid centered approximately 45 km southeast of Motril on Cape Sacratif (Spain). Their subsequent simulated trajectories cover the four-day period from 12:00 UTC, March 26, 2019 to 12:00 UTC, March 30, 2019, and are colored with the elapsed time. They were computed using the MSEAS-PE real-time forecasts of the velocity field over the period of interest and a second-order Runge–Kutta time integration. Most of the parcels southeast of Motril are advected clockwise (initially westward, then toward Cape Sacratif) by the anticyclonic eddy described at the end of the previous subsection (also confirmed by the AVISO reanalyses data). When these parcels approach the Spanish coast, they enter regions with strong vorticity generated in part by the interaction of an eastward coastal current west of Cabo Sacratif with coastal bathymetry, as described in [123]. Such interactions can initiate frontogenesis in this region, which in turn promotes subduction. The remaining few parcels, which are initially located at the western end of the grid, do not advect clockwise, but instead interact with the Atlantic Jet and advect southward [68]. It is clear from the visualization that most parcels remain near the surface for the first 1 to 1.5 days, then subduct afterward. Most trajectories reach depths between

50 m and 100 m, and most subduct along a thin (about 10 km wide) layer along the Spanish coast. Once they complete three-quarters of a circuit around the anticyclone, many of these trajectories then ascend to between 0 m and 50 m depth.

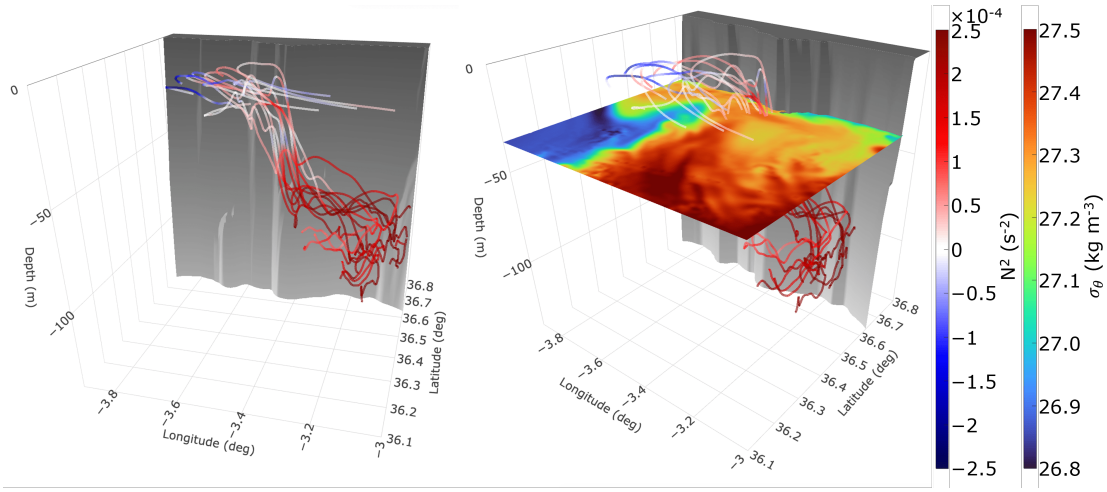

Figure 15: CALYPSO: 3DSeaVizKit visualization of the subset of trajectories from Fig. 14 which are forecast to reach 70 m depth by 12:00 UTC, March 30, 2019. The MSEAS-PE simulated trajectories are colored by the local squared Brunt-Väisälä frequency N^2 (s^{-2}). The right panel additionally shows a depth section of the MSEAS-PE forecast of potential density anomaly field (sigma-theta; $kg\,m^{-3}$) at 35 m depth. These panels reveal a two-stage subduction process which begins with shallow downwelling in unstable surface waters near a front, followed by deeper topographically induced downwelling as the flow passes Cape Sacratif.

Since we are interested in the subduction dynamics, the Boolean filtering capabilities of 3DSeaVizKit allow us to separate the signal from the noise. Figure 15 shows the specific trajectories that reach a depth of 70 m (only 12 trajectories satisfy this condition), colored by the squared Brunt-Väisälä (or buoyancy) frequency N^2, defined as

$$N^2 = -\frac{g}{\rho_0}\frac{\partial \rho}{\partial z}, \tag{2}$$

that describes the oscillation frequency of a parcel of water with density ρ_0 displaced from equilibrium in a stratified background density ρ. With z defined as positive upward, a negative value of N^2 corresponds to locally statically unstable seawater, where higher-density waters reside on top of lower-density waters. The left panel of Figure 15 highlights areas of static instability in blue, neutrally stable water in white, and statically stable water in red. Most downwelling occurs in regions of static instability or neutral stability, in a horizontally thin attracting filament. The right panel of Figure 15 shows the same visualization augmented with a cross-sectional plot of sigma-theta, the potential density anomaly, at 35 m depth. A strong density front is visible along approximately 3.6°W, and it is in this region where the static instability is highest and minor

subduction occurs. This plot also highlights a secondary density front along the Spanish coast (approximately 36.6°N near Motril), where much more significant subduction is forecast to occur at a depth of approximately 20 m to 30 m. Here, the subduction process is induced by topographic interaction as the fluid approaches the bathymetry, resulting in the downward subduction (by as much as 50 m) indicated by the trajectories.

By allowing the user to combine features in a modular way, 3DSeaVizKit allows them to begin with a visualization such as Fig. 14 and interactively create tailored visualizations such as Fig. 15, shedding light on 3D features that would otherwise be challenging to find and understand.

4.4.3. Visualization of Uncertainties

The sensitivity of ocean flow dynamics to small perturbations in the model parameters, initial conditions, and boundary conditions requires quantifying the uncertainties in the forecast [124, 125]. For the CALYPSO real-time experiment, several 300-member ensemble forecasts were issued and one of them covered the period of interest. These probabilistic ocean forecasts were created by applying perturbations to initial conditions downscaled to higher resolution from three models: HYCOM [126, 108], CMEMS [127], and WMOP [120, 121] (1/3 of the realizations used each larger-scale forecast product). This ensemble initialization was completed using ESSE procedures [77, 78, 68]. 3DSeaVizKit was then used to construct a 3D picture of the uncertainty in the ocean fields and dynamics.

Figure 16 shows forecasts of the uncertainties in the velocity field at 18:00 UTC, April 12, 2019 in the full CALYPSO domain shown in black in Figure 5d. The multivariate 3D visualization is split into the western Alboran Sea in Figure 16(a) and the eastern Alboran Sea in Figure 16(b). They show the standard deviation of velocity in horizontal maps at 5 m, 100 m, 250 m, and 450 m depth, and vertical cross-sections located along 3.01°W in the western Alboran Sea and along 2.7°W in the eastern Alboran Sea. In addition, streamtubes of the ensemble mean velocity field at the surface are shown. From the multivariate 3D visualization of the western Alboran Sea in Figure 16(a), we find large forecast uncertainties associated with the position of the Western Alboran Gyre, in addition to significant but lower uncertainties in the Atlantic Jet, a frontal jet of Atlantic waters surrounding the gyre, and especially around the Alboran Ridge (located approximately 36°N, 3°W). For the eastern Alboran Sea shown in Figure 16(b), a smaller, cyclonic eddy is present but weak, with significant uncertainty associated with the location of the intermittent Almería–Oran front.

5. Summary and Conclusions

We presented 3DSeaVizKit, a web-based toolkit for 3D visualization of ocean and geoscience data fields. It enables interactive visualization and exploratory analysis of a wide variety of ocean phenomena using primary and derived field variables. Its development was motivated by the challenge of visualizing the

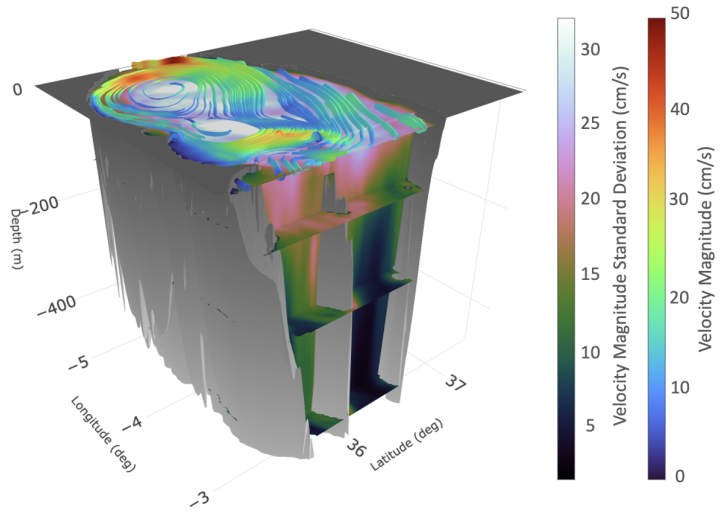

(a) Western Alboran Sea

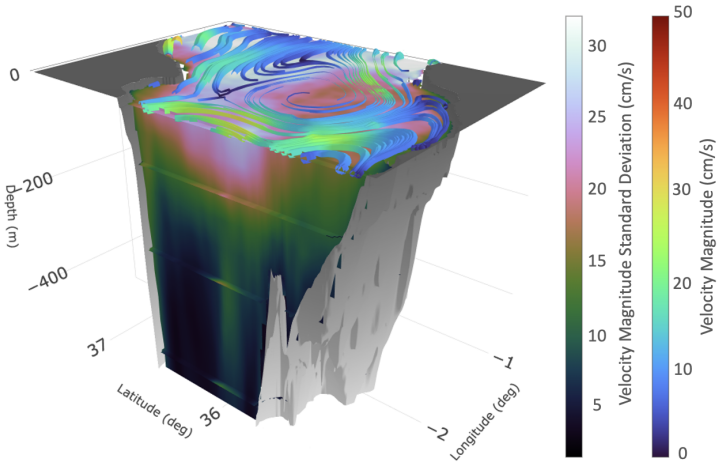

(b) Eastern Alboran Sea

Figure 16: CALYPSO: Multivariate 3D uncertainty visualization using 3DSeaVizKit for the ensemble forecast for April 9-15, 2019, as computed in real-time by our ESSE MSEAS-PE probabilistic modeling system. (a) and (b): Real-time forecasts of the standard deviation of the velocity field ($\mathrm{cm\,s^{-1}}$) at 18:00 UTC, April 12, 2019. The horizontal maps shown are at 5 m, 100 m, 250 m, and 450 m depth, and the vertical cross-section are along 3.01°W in the western Alboran Sea (a) and along 2.7°W in the eastern Alboran Sea (b). Additionally, streamtubes of the ensemble mean surface velocity field forecast are shown, colored by the magnitude of the local ensemble mean velocity ($\mathrm{cm\,s^{-1}}$).

multivariate, multidimensional, and multiresolution outputs of ocean simulations. However, the tool can be extended to support the broader geoscience community.

The 3DSeaVizKit suite provides the user with utilities for plotting scalar,

vector, and trajectory data using lines, cross sections, isosurfaces, and streamtubes. Interactivity and ease of use are key features. Visualizations are served through a web-based GUI built on the Plotly JavaScript library and accelerated through WebGL-enabled graphics processing units. With the tool's modular design, users have control over visualization parameters such as colormap, lighting, domain limits, and section and map locations, and can create new complex visualizations by combining the base features. Applications of 3DSeaVizKit were demonstrated in Massachusetts coastal regions (NSF-ALPHA and BIOMAPS), the Gulf of Mexico (GOM), and the Alboran Sea (CALYPSO).

In the Nantucket and Martha's Vineyard region, 3DSeaVizKit revealed the 3D structures of cold, tidally mixed waters over Nantucket Shoals and their westward transport toward deeper offshore regions. It highlighted submesoscale tilted eddies, meanders, and high-vorticity features associated with the New England shelfbreak front. It also showed the influence of bathymetry on coastal currents, overflows, tidal fronts, and internal waves around Martha's Vineyard and Muskeget Channel, together with associated surface convergence zones and transport barriers. In Massachusetts Bay, 3DSeaVizKit enabled a joint analysis of 3D chlorophyll and ocean-acidification fields. It showed depth-dependent chlorophyll distributions associated with wind-driven upwelling, nutrient supply, internal tides, and advection by the Maine Coastal Current, with subsurface chlorophyll maxima and localized enhancements around Stellwagen Bank. It also exposed mid-depth pH maxima, regions of surface chlorophyll depletion linked to lower-pH waters, and the influence of internal-tide mixing and Gulf of Maine inflows on acidification patterns. In the Gulf of Mexico, the toolkit highlighted the 3D evolution of the Loop Current system and its eddies, including their formation, separation, drift, interaction, and decay. It also exposed the vertical extent and coherence of eddies, streamers, and topographically influenced features, distinguishing structures that spanned hundreds of meters in depth from smaller-scale features confined to the upper ocean. In the Alboran Sea, 3DSeaVizKit showed the structure and variability of gyres, smaller eddies, and coastal recirculations, while highlighting regions of downwelling and subduction as well as the roles of fronts, bathymetry, and instability in this downward transport. It also provided an interactive 3D depiction of forecast uncertainty in major circulation features.

Across all applications, 3DSeaVizKit showed that interactive 3D visualization can reveal coherent structures, transport pathways, circulation features, physical-biogeochemical interactions, subduction processes, and uncertainty patterns that are difficult to infer from isolated 2D views. These capabilities support both scientific discovery and operational oceanography as ocean simulations and observational products continue to increase in complexity and resolution. Future extensions include new multiresolution 3D visualization and integration with mapping software such as Google Maps, in which a coarsened image is continuously refined as the user zooms into an area of interest. Additional developments include uncertainty and risk visualization with large ensemble forecasts [125, 124, 128, 19, 104] as well as location-based and feature-based probability visualization [9, 128]. Other application areas include reachability

and path planning for ocean platforms [53, 129, 105, 130], acoustics forecasting [55, 56, 15, 131], and pollution mitigation and marine ecosystem monitoring [132, 133, 64, 134].

Appendix A. Data Pre-processing: NetCDF files to CSV

In the pre-processing, we split each netCDF file into discrete time steps, placing each time step into a separate CSV file and performing a user-specified level of down-sampling in order to reduce file size. At this point, it is common for the data file to have a non-uniformly spaced grid due to the terrain-following grid employed by many ocean models. Since interpolation on a non-uniformly spaced grid is incredibly slow performance-wise on both a pre-processing and front-end visualizing basis, the pre-processor interpolates each value to a uniform Cartesian grid where the grid spacing is equal. This uniform grid is user-specified and arbitrary; however, forcibly fixing a non-uniformly spaced grid onto an inappropriately matched uniform Cartesian grid can result in a misleading visualization. Therefore, the uniformly interpolated grid must be chosen with consideration of the input data. Finally, the pre-processing pipeline applies a data mask to indicate missing values. Altogether, the pre-processing steps are necessary for the front-end Plotly web framework [34] to display the data properly and efficiently.

Acknowledgments

We are very grateful to the Office of Naval Research (ONR) for research support under grants N00014-18-1-2781 (DRI-CALYPSO) and N00014-19-1-2693 (IN-BDA), to the National Science Foundation (NSF) for support under grant EAR-1520825 (Hazards SEES – ALPHA), to the Understanding Gulf Ocean Systems (UGOS) program of the National Academies of Sciences, Engineering, and Medicine for research support under grant 2018-2798-03, and to Sea Grant and NOAA for support under the grant NA18OAR4170105 (BIOMAPS), each to the Massachusetts Institute of Technology. We also thank all of our DRI-CALYPSO, GOM, and NSF-ALPHA colleagues, as well as everyone who participated in the sea experiments. We thank the Research Science Institute summer program which placed the high school rising senior Mr. Youran Gao as a summer research student with our MSEAS group and spawned this joint work. We thank Manan Doshi for discussions on Lagrangian transport phenomena and all other MSEAS group members for useful feedback.

Data Availability

Ocean simulations data used in this manuscript are available upon request.

References

[1] D. N. Subramani, P. F. J. Lermusiaux, Risk-optimal path planning in stochastic dynamic environments, Computer Methods in Applied Mechanics and Engineering 353 (2019) 391–415. doi:10.1016/j.cma.2019.04.033.

[2] M. Serra, P. Sathe, I. Rypina, A. Kirincich, S. D. Ross, P. Lermusiaux, A. Allen, T. Peacock, G. Haller, Search and rescue at sea aided by hidden flow structures, Nature Communications 11 (2020) 1–7. doi:10.1038/s41467-020-16281-x.

[3] T. Höllt, A. Magdy, P. Zhan, G. Chen, G. Gopalakrishnan, I. Hoteit, C. D. Hansen, M. Hadwiger, Ovis: A framework for visual analysis of ocean forecast ensembles, IEEE Transactions on Visualization and Computer Graphics 20 (8) (2014) 1114–1126. doi:10.1109/TVCG.2014.2307892.

[4] S.-I. Saitoh, R. Mugo, I. N. Radiarta, S. Asaga, F. Takahashi, T. Hirawake, Y. Ishikawa, T. Awaji, T. In, S. Shima, Some operational uses of satellite remote sensing and marine gis for sustainable fisheries and aquaculture, ICES Journal of Marine Science 68 (4) (2011) 687–695.

[5] D. R. Lipşa, R. S. Laramee, S. J. Cox, J. C. Roberts, R. Walker, M. A. Borkin, H. Pfister, Visualization for the physical sciences, Computer Graphics Forum 31 (8) (2012) 2317–2347. doi:10.1111/j.1467-8659.2012.03184.x.

[6] J.-G. Lee, M. Kang, Geospatial big data: challenges and opportunities, Big Data Research 2 (2) (2015) 74–81.

[7] A. Pang, et al., Visualizing uncertainty in geo-spatial data, in: Proceedings of the workshop on the intersections between geospatial information and information technology, Vol. 10, National Research Council Arlington, VA, 2001, p. 3823.

[8] S. Djurcilov, K. Kim, P. F. J. Lermusiaux, A. Pang, Volume rendering data with uncertainty information, in: D. S. Ebert, J. M. Favre, R. Peikert (Eds.), Data Visualization 2001, Joint Eurographics - IEEE TCVG Symposium on Visualization, Springer Vienna, 2001, pp. 243–252, 355–356. doi:10.1007/978-3-7091-6215-6_26.

[9] S. Djurcilov, K. Kim, P. Lermusiaux, A. Pang, Visualizing scalar volumetric data with uncertainty, Computers and Graphics 26 (2) (2002) 239–248. doi:10.1016/S0097-8493(02)00055-9.

[10] H. Guo, W. He, S. Seo, H.-W. Shen, E. M. Constantinescu, C. Liu, T. Peterka, Extreme-scale stochastic particle tracing for uncertain unsteady flow visualization and analysis, IEEE Transactions on Visualization and Computer Graphics 25 (9) (2019) 2710–2724.

[11] D. Jönsson, P. Steneteg, E. Sundén, R. Englund, S. Kottravel, M. Falk, A. Ynnerman, I. Hotz, T. Ropinski, Inviwo — a visualization system with usage abstraction levels, IEEE Transactions on Visualization and Computer Graphics 26 (11) (2020) 3241–3254.

[12] S. Liu, H. Song, Flow visualization with density control, in: Advances in Computer Graphics: 37th Computer Graphics International Conference, CGI 2020, Geneva, Switzerland, October 20–23, 2020, Proceedings, Springer, 2020, pp. 301–312.

[13] W. H. Ali, M. H. Mirhi, A. Gupta, C. S. Kulkarni, C. Foucart, M. M. Doshi, D. N. Subramani, C. Mirabito, P. J. Haley, Jr., P. F. J. Lermusiaux, SeaVizKit: Interactive maps for ocean visualization, in: OCEANS 2019 MTS/IEEE SEATTLE, IEEE, Seattle, 2019, pp. 1–10. doi:10.23919/OCEANS40490.2019.8962794.

[14] D. Fan, T. Liang, H. He, M. Guo, M. Wang, Large-scale oceanic dynamic field visualization based on WebGL, IEEE Access 11 (2023) 82816–82829. doi:10.1109/ACCESS.2023.3301188.

[15] W. H. Ali, A. Charous, C. Mirabito, P. J. Haley, Jr., P. F. J. Lermusiaux, MSEAS-ParEq for ocean-acoustic modeling around the globe, in: OCEANS 2023 IEEE/MTS Gulf Coast, IEEE, Biloxi, MS, 2023, pp. 1–10. doi:10.23919/OCEANS52994.2023.10337377.

[16] P. Lemenkova, Processing oceanographic data by Python libraries Numpy, SciPy and Pandas, Aquatic Research 2 (2) (2019) 73–91. doi:10.3153/AR19009.

[17] K. M. Thyng, C. A. Greene, R. D. Hetland, H. M. Zimmerle, S. F. DiMarco, True colors of oceanography: Guidelines for effective and accurate colormap selection, Oceanography 29 (3) (2016) 9–13. doi:10.5670/oceanog.2016.66.
URL https://doi.org/10.5670/oceanog.2016.66

[18] NCAR (National Center for Atmospheric Research), NCAR graphics (version 6.6.2), Software (Feb. 2019).
URL https://ngwww.ucar.edu/index.html

[19] M. Rautenhaus, M. Böttinger, S. Siemen, R. Hoffman, R. M. Kirby, M. Mirzargar, N. Röber, R. Westermann, Visualization in meteorology—a survey of techniques and tools for data analysis tasks, IEEE Transactions on Visualization and Computer Graphics 24 (12) (2018) 3268–3296. doi:10.1109/TVCG.2017.2779501.

[20] S. Williams, M. Hecht, M. Petersen, R. Strelitz, M. Maltrud, J. Ahrens, M. Hlawitschka, B. Hamann, Visualization and analysis of eddies in a global ocean simulation, Computer Graphics Forum 30 (3) (2011) 991–1000. arXiv:https://onlinelibrary.wiley.com/doi/pdf/10.1111/j.1467-8659.2011.01948.x, doi:https://doi.org/10.1111/j.1467-8659.2011.01948.x.
URL https://onlinelibrary.wiley.com/doi/abs/10.1111/j.1467-8659.2011.01948.x

[21] H. Childs, E. Brugger, B. Whitlock, J. Meredith, S. Ahern, D. Pugmire, K. Biagas, M. Miller, C. Harrison, et al., VisIt: An end-user tool for visualizing and analyzing very large data, High Performance Visualization—Enabling Extreme-Scale Scientific Insight (2012) 357–372.

[22] J. Ahrens, B. Geveci, C. Law, ParaView: An end-user tool for large-data visualization, in: C. D. Hansen, C. R. Johnson (Eds.), Visualization Handbook, Butterworth-Heinemann, Burlington, 2005, pp. 717–731.

doi:https://doi.org/10.1016/B978-012387582-2/50038-1.
URL https://www.sciencedirect.com/science/article/pii/B9780123875822500381

[23] P. Nandakishore, N. S. Nair, P. D. Alapatt, T. Kurian, K. G. Preetha, A Python framework for interactive 3D visualisation of ocean data, in: V. S. Reddy, J. Wang, K. T. V. Reddy (Eds.), Soft Computing and Signal Processing, Springer, Singapore, 2024, pp. 541–553. doi:10.1007/978-981-99-8628-6_46.

[24] K. G. Preetha, S. Saritha, J. Jeevan, K. A. Anoop, P. A. Maheswaran, OCEANVIZIO: A dynamic and scalable visualization tool for comprehensive analysis of ocean parameters, Defence Science Journal 75 (6) (2025) 685–692. doi:10.14429/dsj.21345.

[25] C. Hörath, D. Derichs, L. Eyl, O. Kallenberg, T. Gerrits, DeepSwitch - a web-based tool for the introduction to visual analysis of spatiotemporal processes in oceanographic data, in: K. Feige, B. Nsonga, K. Rink (Eds.), Workshop on Visualisation in Environmental Sciences (EnvirVis), The Eurographics Association, 2025, pp. 1–8. doi:10.2312/envirvis.20251146.

[26] A. Coscia, H. M. Sapers, N. Deutsch, M. Khurana, J. S. Magyar, S. A. Parra, D. R. Utter, R. L. Wipfler, D. W. Caress, E. J. Martin, J. B. Paduan, M. Hendrie, S. Lombeyda, H. Mushkin, A. Endert, S. Davidof, V. J. Orphan, DeepSee: Multidimensional visualizations of seabed ecosystems, in: Proceedings of the 2024 CHI Conference on Human Factors in Computing Systems, Honolulu, 2024, pp. 1–16. doi:10.1145/3613904.3642001.

[27] A. Ismail, S. N. A. Jawaddi, F. H. Sazali, J. M. Zain, J. Jaafar, M. H. Hasan, I. A. Aziz, N. S. Haron, A comprehensive review of interactive visualization for MetOcean domain, Journal of Visualization 28 (5) (2025) 937–962. doi:10.1007/s12650-025-01077-2.

[28] R. Schlitzer, Interactive analysis and visualization of geoscience data with ocean data view, Computers & Geosciences 28 (10) (2002) 1211 – 1218, shareware and freeware in the Geosciences II. A special issue in honour of John Butler. doi:https://doi.org/10.1016/S0098-3004(02)00040-7.
URL http://www.sciencedirect.com/science/article/pii/S0098300402000407

[29] M. Rautenhaus, M. Kern, A. Schäfler, R. Westermann, Three-dimensional visualization of ensemble weather forecasts – part 1: The visualization tool Met.3D (version 1.0), Geoscientific Model Development 8 (7) (2015) 2329–2353. doi:10.5194/gmd-8-2329-2015.
URL https://www.geosci-model-dev.net/8/2329/2015/

[30] C. Helbig, L. Bilke, H.-S. Bauer, M. Böttinger, O. Kolditz, MEVA-an interactive visualization application for validation of multifaceted meteorological data with multiple 3d devices, PloS one 10 (4) (2015) e0123811.

[31] M. Koutek, F. Debie, I. Van der Neut, 3D exploration of meteorological data: Facing the challenges of operational forecasters, in: EGU General Assembly Conference Abstracts, 2016, pp. EPSC2016–8398.

[32] W. L. Hibbard, J. Anderson, I. Foster, B. E. Paul, R. Jacob, C. Schafer, M. K. Tyree, Exploring coupled atmosphere-ocean models using Vis5D, The International Journal of High Performance Computing Applications 10 (2–3) (1996) 211—-222. doi:10.1177/109434209601000208.

[33] S. Li, S. Jaroszynski, S. Pearse, L. Orf, J. Clyne, VAPOR: A visualization package tailored to analyze simulation data in earth system science, Atmosphere 10 (9) (2019). doi:10.3390/atmos10090488.
URL https://www.mdpi.com/2073-4433/10/9/488

[34] Plotly (Aug. 2023). [link].
URL https://plotly.com/

[35] W. H. Ali, Y. Gao, C. Foucart, M. Doshi, C. Mirabito, P. J. Haley, Jr., P. F. J. Lermusiaux, High-performance visualization for ocean modeling, in: OCEANS 2022 IEEE/MTS, IEEE, Hampton Roads, VA, 2022, pp. 1–10. doi:10.1109/OCEANS47191.2022.9977075.

[36] MSEAS (Multidisciplinary Simulation, Estimation, and Assimilation Systems) Group, Software (Aug. 2011).
URL http://mseas.mit.edu/software/

[37] P. J. Haley, Jr., P. F. J. Lermusiaux, Multiscale two-way embedding schemes for free-surface primitive equations in the "Multidisciplinary Simulation, Estimation and Assimilation System", Ocean Dynamics 60 (6) (2010) 1497–1537. doi:10.1007/s10236-010-0349-4.

[38] P. F. J. Lermusiaux, P. J. Haley, W. G. Leslie, A. Agarwal, O. Logutov, L. J. Burton, Multiscale physical and biological dynamics in the Philippine Archipelago: Predictions and processes, Oceanography 24 (1) (2011) 70–89, Special Issue on the Philippine Straits Dynamics Experiment. doi:10.5670/oceanog.2011.05.

[39] P. J. Haley, Jr., A. Agarwal, P. F. J. Lermusiaux, Optimizing velocities and transports for complex coastal regions and archipelagos, Ocean Modelling 89 (2015) 1–28. doi:10.1016/j.ocemod.2015.02.005.

[40] O. G. Logutov, P. F. J. Lermusiaux, Inverse barotropic tidal estimation for regional ocean applications, Ocean Modelling 25 (1–2) (2008) 17–34. doi:10.1016/j.ocemod.2008.06.004.

[41] P. F. J. Lermusiaux, A. R. Robinson, Data assimilation via Error Subspace Statistical Estimation, part I: Theory and schemes, Monthly Weather Review 127 (7) (1999) 1385–1407. doi:10.1175/1520-0493(1999)127<1385:DAVESS>2.0.CO;2.

[42] P. F. J. Lermusiaux, Data assimilation via Error Subspace Statistical Estimation, part II: Mid-Atlantic Bight shelfbreak front simulations, and ESSE validation, Monthly Weather Review 127 (7) (1999) 1408–1432. doi:10.1175/1520-0493(1999)127<1408:DAVESS>2.0.CO;2.

[43] P. F. J. Lermusiaux, Estimation and study of mesoscale variability in the Strait of Sicily, Dynamics of Atmospheres and Oceans 29 (2) (1999) 255–303. doi:10.1016/S0377-0265(99)00008-1.

[44] P. F. J. Lermusiaux, Adaptive modeling, adaptive data assimilation and adaptive sampling, Physica D: Nonlinear Phenomena 230 (1) (2007) 172–196. doi:10.1016/j.physd.2007.02.014.

[45] O. Schofield, S. Glenn, J. Orcutt, M. Arrott, M. Meisinger, A. Gangopadhyay, W. Brown, R. Signell, M. Moline, Y. Chao, S. Chien, D. Thompson, A. Balasuriya, P. F. J. Lermusiaux, M. Oliver, Automated sensor networks to advance ocean science, Eos Trans. AGU 91 (39) (2010) 345–346. doi:10.1029/2010EO390001.

[46] C. Evangelinos, P. F. J. Lermusiaux, J. Xu, P. J. Haley, C. N. Hill, Many task computing for real-time uncertainty prediction and data assimilation in the ocean, IEEE Transactions on Parallel and Distributed Systems 22 (6) (2011) 1012–1024, Special Section on Many-Task Computing. doi:10.1109/TPDS.2011.64.

[47] Ş. T. Beşiktepe, P. F. J. Lermusiaux, A. R. Robinson, Coupled physical and biogeochemical data-driven simulations of Massachusetts Bay in late summer: Real-time and post-cruise data assimilation, Journal of Marine Systems 40–41 (2003) 171–212. doi:10.1016/S0924-7963(03)00018-6.

[48] J. Coulin, P. J. Haley, Jr., S. Jana, C. S. Kulkarni, P. F. J. Lermusiaux, T. Peacock, Environmental ocean and plume modeling for deep sea mining in the Bismarck Sea, in: Oceans 2017 - Anchorage, Anchorage, AK, 2017, pp. 1–10.

[49] C. S. Kulkarni, P. J. Haley, Jr., P. F. J. Lermusiaux, A. Dutt, A. Gupta, C. Mirabito, D. N. Subramani, S. Jana, W. H. Ali, T. Peacock, C. M. Royo, A. Rzeznik, R. Supekar, Real-time sediment plume modeling in the Southern California Bight, in: OCEANS Conference 2018, IEEE, Charleston, SC, 2018, pp. 1–10. doi:10.1109/OCEANS.2018.8653642.

[50] P. F. J. Lermusiaux, F. Lekien, Dynamics and Lagrangian coherent structures in the ocean and their uncertainty, in: J. E. Marsden, J. Scheurle (Eds.), Extended Abstract in report of the Dynamical System Methods in Fluid Dynamics Oberwolfach Workshop, Mathematisches Forschungsinstitut Oberwolfach, Germany, 2005, p. 2. doi:10.1121/1.2988093.

[51] C. S. Kulkarni, P. F. J. Lermusiaux, Advection without compounding errors through flow map composition, Journal of Computational Physics 398 (2019) 108859. doi:10.1016/j.jcp.2019.108859.

[52] P. F. J. Lermusiaux, T. Lolla, P. J. Haley, Jr., K. Yigit, M. P. Ueckermann, T. Sondergaard, W. G. Leslie, Science of autonomy: Time-optimal path planning and adaptive sampling for swarms of ocean vehicles, in: T. Curtin (Ed.), Springer Handbook of Ocean Engineering: Autonomous Ocean Vehicles, Subsystems and Control, Springer, 2016, Ch. 21, pp. 481–498. doi:10.1007/978-3-319-16649-0_21.

[53] P. F. J. Lermusiaux, D. N. Subramani, J. Lin, C. S. Kulkarni, A. Gupta, A. Dutt, T. Lolla, P. J. Haley, Jr., W. H. Ali, C. Mirabito, S. Jana, A future for intelligent autonomous ocean observing systems, Journal of Marine Research 75 (6) (2017) 765–813, the Sea. Volume 17, The Science of Ocean Prediction, Part 2. doi:10.1357/002224017823524035.

[54] P. F. J. Lermusiaux, J. Xu, C.-F. Chen, S. Jan, L. Chiu, Y.-J. Yang, Coupled ocean–acoustic prediction of transmission loss in a continental shelfbreak region: Predictive skill, uncertainty quantification, and dynamical sensitivities, IEEE Journal of Oceanic Engineering 35 (4) (2010) 895–916. doi:10.1109/JOE.2010.2068611.

[55] P. F. J. Lermusiaux, P. J. Haley, Jr., C. Mirabito, W. H. Ali, M. Bhabra, P. Abbot, C.-S. Chiu, C. Emerson, Multi-resolution probabilistic ocean physics-acoustic modeling: Validation in the New Jersey continental shelf, in: OCEANS 2020 IEEE/MTS, IEEE, 2020, pp. 1–9. doi:10.1109/IEEECONF38699.2020.9389193.

[56] P. F. J. Lermusiaux, C. Mirabito, P. J. Haley, Jr., W. H. Ali, A. Gupta, S. Jana, E. Dorfman, A. Laferriere, A. Kofford, G. Shepard, M. Goldsmith, K. Heaney, E. Coelho, J. Boyle, J. Murray, L. Freitag, A. Morozov, Real-time probabilistic coupled ocean physics-acoustics forecasting and data assimilation for underwater GPS, in: OCEANS 2020 IEEE/MTS, IEEE, 2020, pp. 1–9. doi:10.1109/IEEECONF38699.2020.9389003.

[57] S. C. Shadden, F. Lekien, J. E. Marsden, Definition and properties of lagrangian coherent structures from finite-time lyapunov exponents in two-dimensional aperiodic flows, Physica D: Nonlinear Phenomena 212 (3) (2005) 271–304. doi:https://doi.org/10.1016/j.physd.2005.10.007.
URL https://www.sciencedirect.com/science/article/pii/S0167278905004446

[58] T. Wilde, C. Rossi, H. Theisel, Recirculation surfaces for flow visualization, IEEE Transactions on Visualization & Computer Graphics 25 (01) (2019) 946–955. doi:10.1109/TVCG.2018.2864813.

[59] L. Hofmann, VCG - Double Gyre 3D (2019).
URL https://vcg.iwr.uni-heidelberg.de/plugins/vcg_-_double_gyre_3d

[60] C. Coulliette, S. Wiggins, Intergyre transport in a wind-driven, quasigeostrophic double gyre: An application of lobe dynamics, Nonlinear Processes in Geophysics 7 (1/2) (2000) 59–85. doi:10.5194/npg-7-59-2000.
URL https://npg.copernicus.org/articles/7/59/2000/

[61] C. Coulliette, F. Lekien, J. D. Paduan, G. Haller, J. E. Marsden, Optimal pollution mitigation in monterey bay based on coastal radar data and nonlinear dynamics, Environmental science & technology 41 (18) (2007) 6562–6572.

[62] P. J. Haley, Jr., S. Jana, C. Mirabito, C. S. Kulkarni, A. Dutt, A. Gupta, W. H. Ali, P. F. J. Lermusiaux, Advanced Lagrangian predictions for hazards assessments: Real-time pilot experiment, Ocean ModellingIn preparation (2026).

[63] MSEAS ALPHA Ex., NSF-ALPHA real-time sea exercise 2018: Nantucket and Martha's Vineyard - August 2018 (Aug. 2018).
URL http://mseas.mit.edu/Sea_exercises/NSF_ALPHA/2018/

[64] P. J. Haley, Jr., A. Gupta, C. Mirabito, P. F. J. Lermusiaux, Towards Bayesian ocean physical-biogeochemical-acidification prediction and learning systems for Massachusetts Bay, in: OCEANS 2020 IEEE/MTS, IEEE, 2020, pp. 1–9. doi:10.1109/IEEECONF38699.2020.9389210.

[65] MSEAS BIOMAPS, Bayesian intelligent ocean modeling and acidification prediction systems (BIOMAPS) project (Jul. 2019).
URL http://mseas.mit.edu/Research/BIOMAPS/

[66] P. J. Haley, Jr., C. Mirabito, M. Doshi, P. F. J. Lermusiaux, Ensemble forecasting for the Gulf of Mexico Loop Current region, in: OCEANS 2023 IEEE/MTS Gulf Coast, IEEE, Biloxi, MS, 2023, pp. 1–10. doi:10.23919/OCEANS52994.2023.10337035.

[67] MSEAS GoMex, Understanding and predicting the Gulf of Mexico Loop Current project (Dec. 2018).
URL http://mseas.mit.edu/Research/LoopCurrent/

[68] C. Mirabito, P. J. Haley, Jr., M. Doshi, K. Gkirgkis, W. H. Ali, C. Kulkarni, A. Gupta, P. F. J. Lermusiaux, A. Mahadevan, M. Freilich, M. Dever, S. Johnston, T. Özgökmen, L. Pratt, I. Rypina, D. Rudnick, A. Shcherbina, C. McNeil, R. Musgrave, S. Sarkar, L. Centurioni, E. D'Asaro, J. McWilliams, P. Sullivan, H. Huntley, D. Kirwan, T. Farrar, A. Griffa, U. Send, M. Lankhorst, M. Allshouse, T. Peacock, P.-M. Poulain, S. Ruiz, A. Pascual, J. Tintoré, J. Allen, B. Mourre, M. Garcia-Jove, E. Alou-Font, N. Zarakanellos, C. Muñoz, I. Ruiz, A. Z. Worden, Real-time high-resolution probabilistic Eulerian and Lagrangian forecasting in the Alboran Sea: Skill, subduction, and multi-downscaling ensemble predictions, Ocean ModellingIn preparation (2026).

[69] MSEAS CALYPSO Ex., CALYPSO real-time sea experiment 2019: Alboran Sea – March - April 2019, Accessed 2025-01-30 (Apr. 2019).
URL http://mseas.mit.edu/Sea_exercises/CALYPSO/2019/

[70] GEBCO Bathymetric Compilation Group, The GEBCO_2022 grid - a continuous terrain model of the global oceans and land, Dataset (Jun. 2022). doi:10.5285/e0f0bb80-ab44-2739-e053-6c86abc0289c.

[71] E. R. Twomey, R. P. Signell, Construction of a 3-arcsecond digital elevation model for the gulf of maine, Open-File Report 2011-1127, U.S. Geological Survey, Coastal and Marine Geology Program, Woods Hole Coastal and Marine Science Center, Woods Hole, MA (2013).
URL https://pubs.usgs.gov/of/2011/1127/

[72] NOAA Fisheries, 2010-2019 hydrographic conditions of the northeast U.S. continental shelf: Conductivity-temperature-depth (CTD) reports (Nov. 2020).
URL https://www.fisheries.noaa.gov/resource/data/2010-2019-hydrographic-conditions-northeast-us-continental-shelf-conductivity

[73] T. P. Boyer, O. K. Baranova, C. Coleman, H. E. Garcia, A. Grodsky, R. A. Locarnini, A. V. Mishonov, C. R. Paver, J. R. Reagan, D. Seidov, I. V. Smolyar, K. W. Weathers, M. M. Zweng, World Ocean Database 2018, NCEI, Silver Spring, MD, a. V. Mishonov, Technical Ed., NOAA Atlas NESDIS 87 (2018).
URL https://www.ncei.noaa.gov/sites/default/files/2020-04/wod_intro_0.pdf

[74] A. Gangopadhyay, A. R. Robinson, Feature-oriented regional modeling of oceanic fronts, Dynamics of Atmospheres and Oceans 36 (1) (2002) 201–232,

ocean Fronts. doi:https://doi.org/10.1016/S0377-0265(02)00032-5.
URL https://www.sciencedirect.com/science/article/pii/S0377026502000325

[75] A. Gangopadhyay, A. R. Robinson, P. J. Haley, W. G. Leslie, C. J. Lozano, J. J. Bisagni, Z. Yu, Feature-oriented regional modeling and simulations in the gulf of maine and georges bank, Continental Shelf Research 23 (3-4) (2003) 317–353.

[76] JHU APL Ocean Remote Sensing Group, Advanced high resolution radiometer (AVHRR) imagery (Aug. 2017).
URL http://fermi.jhuapl.edu/avhrr/cmo/17aug/index_thumb.html

[77] P. F. J. Lermusiaux, D. G. M. Anderson, C. J. Lozano, On the mapping of multivariate geophysical fields: Error and variability subspace estimates, Quarterly Journal of the Royal Meteorological Society 126 (565) (2000) 1387–1429. doi:10.1256/smsqj.56509.

[78] P. F. J. Lermusiaux, On the mapping of multivariate geophysical fields: Sensitivities to size, scales, and dynamics, Journal of Atmospheric and Oceanic Technology 19 (10) (2002) 1602–1637. doi:10.1175/1520-0426(2002)019<1602:OTMOMG>2.0.CO;2.

[79] NOAA NCEP (National Centers for Environmental Prediction), NOAA/NCEP North American Mesoscale forecast system (NAM) (Aug. 2023).
URL https://www.emc.ncep.noaa.gov/emc/pages/numerical_forecast_systems/nam.php

[80] G. D. Egbert, S. Y. Erofeeva, Efficient inverse modeling of barotropic ocean tides, Journal of Atmospheric and Oceanic Technology 19 (2) (2002) 183–204. doi:10.1175/1520-0426(2002)019<0183:EIMOBO>2.0.CO;2.

[81] G. D. Egbert, S. Y. Erofeeva, OSU tidal inversion, http://volkov.oce.orst.edu/tides/tpxo8_atlas.html (2013).

[82] R. He, J. L. Wilkin, Barotropic tides on the southeast new england shelf: A view from a hybrid data assimilative modeling approach, Journal of Geophysical Research: Oceans 111 (C8) (2006).

[83] G. Haller, Lagrangian coherent structures, Annual Review of Fluid Mechanics 47 (1) (2015) 137–162. arXiv:https://doi.org/10.1146/annurev-fluid-010313-141322, doi:10.1146/annurev-fluid-010313-141322.
URL https://doi.org/10.1146/annurev-fluid-010313-141322

[84] T. Peacock, G. Haller, Lagrangian coherent structures: The hidden skeleton of fluid flows, Physics today 66 (2) (2013) 41.

[85] M. M. Doshi, C. S. Kulkarni, W. H. Ali, A. Gupta, P. F. J. Lermusiaux, P. Zhan, I. Hoteit, O. Knio, Flow maps and coherent sets for characterizing residence times and connectivity in lagoons and coral reefs: The case of the Red Sea, in: OCEANS 2019 MTS/IEEE SEATTLE, IEEE, Seattle, 2019, pp. 1–8. doi:10.23919/OCEANS40490.2019.8962643.

[86] C. S. Kulkarni, P. F. J. Lermusiaux, Persistent Lagrangian material coherence in fluid and ocean flows using flow map composition, in preparation (2026).

[87] P. F. J. Lermusiaux, P. J. Haley, Jr., C. Mirabito, Lagrangian flow map analysis of ocean dynamics and material transports, in: OCEANS 2025 IEEE/MTS Great Lakes, IEEE, Chicago, 2025, pp. 1–10. doi:10.23919/OCEANS59106.2025.11244986.

[88] P. F. J. Lermusiaux, P. J. Haley, Jr, N. K. Yilmaz, Environmental prediction, path planning and adaptive sampling: Sensing and modeling for efficient ocean monitoring, management and pollution control, Sea Technology 48 (9) (2007) 35–38.

[89] K. Fennel, M. Gehlen, P. Brasseur, C. W. Brown, S. Ciavatta, G. Cossarini, A. Crise, C. A. Edwards, D. Ford, M. A. Friedrichs, et al., Advancing marine biogeochemical and ecosystem reanalyses and forecasts as tools for monitoring and managing ecosystem health, Frontiers in Marine Science 6 (2019) 89.

[90] J. C. Orr, V. J. Fabry, O. Aumont, L. Bopp, S. C. Doney, R. A. Feely, A. Gnanadesikan, N. Gruber, A. Ishida, F. Joos, R. M. Key, K. Lindsay, E. Maier-Reimer, R. Matear, P. Monfray, A. Mouchet, R. G. Najjar, G.-K. Plattner, K. B. Rodgers, C. L. Sabine, J. L. Sarmiento, R. Schlitzer, R. D. Slater, I. J. Totterdell, M.-F. Weirig, Y. Yamanaka, A. Yool, Anthropogenic ocean acidification over the twenty-first century and its impact on calcifying organisms, Nature 437 (7059) (2005) 681–686.

[91] R. A. Feely, C. L. Sabine, J. M. Hernandez-Ayon, D. Ianson, B. Hales, Evidence for upwelling of corrosive" acidified" water onto the continental shelf, science 320 (5882) (2008) 1490–1492.

[92] V. J. Fabry, B. A. Seibel, R. A. Feely, J. C. Orr, Impacts of ocean acidification on marine fauna and ecosystem processes, ICES Journal of Marine Science 65 (3) (2008) 414–432. arXiv:https://academic.oup.com/icesjms/article-pdf/65/3/414/29130917/fsn048.pdf, doi:10.1093/icesjms/fsn048.
URL https://doi.org/10.1093/icesjms/fsn048

[93] J. A. Cummings, O. M. Smedstad, Variational Data Assimilation for the Global Ocean, Springer Berlin Heidelberg, Berlin, Heidelberg, 2013, pp. 303–343. doi:10.1007/978-3-642-35088-7_13.

[94] P. F. J. Lermusiaux, C. Evangelinos, R. Tian, P. J. Haley, Jr, J. J. McCarthy, N. M. Patrikalakis, A. R. Robinson, H. Schmidt, Adaptive coupled physical and biogeochemical ocean predictions: A conceptual basis, in: Computational Science - ICCS 2004, Vol. 3038 of Lecture Notes in Computer Science, Springer Berlin Heidelberg, 2004, pp. 685–692. doi:10.1007/978-3-540-24688-6_89.

[95] C. Hauri, N. Gruber, M. Vogt, S. C. Doney, R. A. Feely, Z. Lachkar, A. Leinweber, A. M. P. McDonnell, M. Münnich, G.-K. Plattner, Spatiotemporal variability and long-term trends of ocean acidification in the California Current System, Biogeosciences 10 (1) (2013) 193–216.

[96] E. R. Lewis, D. W. R. Wallace, Program Developed for CO_2 System Calculations, Tech. Rep. CDIAC-105, Oak Ridge National Laboratory, Oak Ridge, Tennessee (1998). doi:10.15485/1464255.
URL https://www.nodc.noaa.gov/ocads/oceans/CO2SYS/co2rprt.html

[97] T.-H. Peng, C. Langdon, Gulf of Mexico and East Coast Carbon Cruise (GOMECC), Tech. Rep. RB-07-05, NOAA Atlantic Oceanographic and Meteorological Laboratory (2007).
URL https://www.aoml.noaa.gov/ocd/gcc/GOMECC1/CruiseReportfinal.pdf

[98] R. Wanninkhof, M. Wood, L. Barbero, Gulf of Mexico and East Coast Carbon Cruise #2 (GOMECC-2), Tech. rep., NOAA Atlantic Oceanographic and Meteorological Laboratory (2012).
URL https://www.aoml.noaa.gov/ocd/gcc/GOMECC2/Cruise_Report_June2014.pdf

[99] P. F. J. Lermusiaux, Evolving the subspace of the three-dimensional multiscale ocean variability: Massachusetts Bay, Journal of Marine Systems 29 (1) (2001) 385–422. doi:10.1016/S0924-7963(01)00025-2.

[100] Z. A. Wang, G. L. Lawson, C. H. Pilskaln, A. E. Maas, Seasonal controls of aragonite saturation states in the gulf of maine, Journal of Geophysical Research: Oceans 122 (1) (2017) 372–389. doi:https://doi.org/10.1002/2016JC012373.
URL https://agupubs.onlinelibrary.wiley.com/doi/abs/10.1002/2016JC012373

[101] NAS (National Academies of Sciences, Engineering, and Medicine), Understanding and Predicting the Gulf of Mexico Loop Current: Critical Gaps and Recommendations, National Academies Press, Washington, DC, 2018. doi:10.17226/24823.

[102] OOM (Ocean Observing and Modeling) Group (He et al.), Understanding and predicting the Gulf of Mexico Loop Current, topic 8: Numerical modeling (2018).
URL http://oomg.meas.ncsu.edu/index.php/projects/ugos/

[103] D. S. Dukhovskoy, E. P. Chassignet, A. Bozec, S. L. Morey, Assessment of predictability of the loop current in the gulf of mexico from observing system experiments and observing system simulation experiments, Frontiers in Marine Science 10 (2023). doi:10.3389/fmars.2023.1153824.

[104] P. F. J. Lermusiaux, P. J. Haley, Jr., C. Mirabito, E. M. Mule, S. F. DiMarco, A. Dancer, X. Ge, A. H. Knap, Y. Liu, S. Mahmud, U. C. Nwankwo, S. Glenn, T. N. Miles, D. Aragon, K. Coleman, M. Smith, M. Leber, R. Ramos, J. Storie, G. Stuart, J. Marble, P. Barros, E. P. Chassignet, A. Bower, H. H. Furey, B. Jaimes de la Cruz, L. K. Shay, M. Tenreiro, E. Pallàs Sanz, J. Sheinbaum, P. Pérez Brunius, D. Wilson, J. van Smirren, R. Monreal Jiménez, D. A. Salas de León, V. K. Contreras Tereza, M. Feldman, M. Khadka, Real-time ocean probabilistic forecasts, reachability analysis, and adaptive sampling in the Gulf of Mexico, in: OCEANS 2024 IEEE/MTS Halifax, IEEE, Halifax, 2024, pp. 1–10. doi:10.1109/OCEANS55160.2024.10754153.

[105] E. M. Mule, P. J. Haley, C. Mirabito, S. F. DiMarco, S. Mahmud, A. Dancer, X. Ge, A. H. Knap, Y. Liu, U. C. Nwankwo, S. Glenn, T. N. Miles, D. Aragon, K. Coleman, M. Smith, M. Leber, R. Ramos, J. Storie, G. Stuart, J. Marble, P. Barros, E. P. Chassignet, A. Bower, H. H. Furey, B. Jaimes de la Cruz, L. K. Shay, M. Tenreiro, E. Pallàs Sanz, J. Sheinbaum, P. Pérez Brunius, D. Wilson, J. van Smirren, R. Monreal Jiménez, D. A. Salas de León, V. K. Contreras Tereza, M. Feldman, M. Khadka, P. F. J. Lermusiaux, Real-time probabilistic reachability forecasting for gliders in the Gulf of Mexico, in: OCEANS 2024 IEEE/MTS Halifax, IEEE, Halifax, 2024, pp. 1–10. doi:10.1109/OCEANS55160.2024.10754057.

[106] C. Mirabito, P. J. Haley, Jr., E. M. Mule, A. V. Rodriguez, S. L. Morey, E. P. Chassignet, S. M. Glenn, T. N. Miles, D. Aragon, K. Coleman, M. Smith, S. F. DiMarco, S. Mahmud, X. Ge, A. H. Knap, B. J. de la Cruz, L. K. Shay, M. Leber, R. Ramos, H. Nowak, J. Storie, A. Romer, M. Tenreiro, E. Pallàs-Sanz, J. Sheinbaum, P. Pérez-Brunius, R. He, Y. Deng, T. Wu, A. Bower, H. H. Furey, K. A. Donohue, J. van Smirren, P. Hogan, G. Jacobs, M. Feldman, F. K. Wiese, M. Khadka, P. F. J. Lermusiaux, Real-time optimal planning and adaptive sampling for multi-platform operations in the Gulf of Mexico, in: OCEANS 2025 IEEE/MTS Great Lakes, IEEE, Chicago, 2025, pp. 1–10. doi:10.23919/OCEANS59106.2025.11245042.

[107] S. Saha, S. Moorthi, X. Wu, J. Wang, S. Nadiga, T. Patrick, D. Behringer, Y.-T. Hou, H.-y. Chuang, M. Iredell, M. Ek, J. Meng, R. Yang, M. P. n. Mendez, H. van den Dool, Q. Zhang, W. Wang, M. Chen, E. Becker, The NCEP climate forecast system version 2, Journal of Climate 27 (6) (2014) 2185–2208. doi:10.1175/jcli-d-12-00823.1.

[108] HYCOM Consortium, HYbrid Coordinate Ocean Model (HYCOM) (Feb. 2023). URL https://hycom.org

[109] N. Sharma, J. S. Storie, K. M. Obenour, M. J. Leber, A. Srinivasan, Loop Current hyperactivity: Analysis of in situ measurements in the Gulf of Mexico, in: Offshore Technology Conference, Houston, TX, 2016. doi:10.4043/27229-MS.

[110] L. Hiron, P. Miron, L. K. Shay, W. E. Johns, E. P. Chassignet, A. Bozec, Lagrangian coherence and source of water of Loop Current Frontal eddies in the Gulf of Mexico, Progress in Oceanography 208 (2022) 102876. doi:10.1016/j.pocean.2022.102876.

[111] A. Mahadevan, A. Pascual, D. L. Rudnick, S. Ruiz, J. Tintoré, E. D'Asaro, Coherent pathways for vertical transport from the surface ocean to interior, Bulletin of the American Meteorological Society 101 (11) (2020) E1996–E2004.

[112] A. Mahadevan, E. D'Asaro, J. Allen, P. Almaraz García, E. Alou-Font, H. M. Aravind, P. Balaguer, I. Caballero, N. Calafat, A. Carbornero, B. Casas, C. Castilla, L. Centurioni, M. Conley, G. Cristofano, E. Cutolo, M. Dever, A. E. Navarro, F. M. Falcieri, M. Freilich, E. Goodwin, R. Graham, C. Guigand, B. Hodges, H. Huntley, S. Johnston, M. Lankhorst, P. Lermusiaux, I. Lizaran, C. Mirabito, A. Miralles, B. Mourre, G. Navarro, M. Ohmart, S. Ouala, T. Özgökmen, A. Pascual, J. H. Pou, P.-M. Poulain, A. Ren, D. Rodríguez Tarry, D. Rudnick, M. Rubio, S. Ruiz, I. Rypina, J. Tintoré, U. Send, A. Shcherbina,

M. Torner, G. S. Vieira, N. Wirth, N. Zarokanellos, CALYPSO 2019 cruise report: Field campaign in the Mediterranean, Technical Report WHOI-2020-02, Woods Hole Oceanographic Institution, Woods Hole, MA (Jan. 2020). doi:10.1575/1912/25266.

[113] MSEAS CALYPSO, Coherent Lagrangian pathways from the surface ocean to interior (CALYPSO) project (Nov. 2018).
URL http://mseas.mit.edu/Research/CALYPSO/

[114] WHOI CALYPSO (Mahadevan et al.), Coherent Lagrangian pathways from the surface ocean to interior project (2018).
URL https://calypsodri.whoi.edu/

[115] M. Garcia-Jove, B. Mourre, N. D. Zarokanellos, P. F. J. Lermusiaux, D. L. Rudnick, J. Tintoré, Frontal dynamics in the Alboran Sea: 2. Processes for vertical velocities development, Journal of Geophysical Research: Oceans 127 (3) (2022) e2021JC017428. doi:10.1029/2021JC017428.

[116] H. M. Aravind, V. Verma, S. Sarkar, M. A. Freilich, A. Mahadevan, P. J. Haley, Jr., P. F. J. Lermusiaux, M. R. Allshouse, Lagrangian surface signatures reveal upper-ocean vertical displacement conduits near oceanic density fronts, Ocean Modelling 181 (2023) 102136. doi:10.1016/j.ocemod.2022.102136.

[117] C. J. Olson, J. J. Becker, D. T. Sandwell, A new global bathymetry map at 15 arcsecond resolution for resolving seafloor fabric: SRTM15_PLUS, in: AGU Fall Meeting, American Geophysical Union, San Francisco, 2014, pp. OS34A–03.

[118] C. J. Olson, J. J. Becker, D. T. Sandwell, SRTM15_PLUS: Data fusion of Shuttle Radar Topography Mission (SRTM) land topography with measured and estimated seafloor topography, Dataset, NCEI Accession 0150537 (May 2016).

[119] B. Tozer, D. T. Sandwell, W. H. F. Smith, C. Olson, J. R. Beale, P. Wessel, Global bathymetry and topography at 15 arc sec: SRTM15+, Earth and Space Science 6 (10) (2019) 1847–1864. doi:10.1029/2019EA000658.

[120] M. Juza, B. Mourre, L. Renault, S. Gómara, K. Sebastián, S. Lora, J. P. Beltran, B. Frontera, B. Garau, C. Troupin, M. Torner, E. Heslop, B. Casas, R. Escudier, G. Vizoso, J. Tintoré, SOCIB operational ocean forecasting system and multi-platform validation in the western Mediterranean Sea, Journal of Operational Oceanography 9 (S1) (2016) s155–s166. doi:10.1080/1755876X.2015.1117764.

[121] B. Mourre, E. Aguiar, M. Juza, J. Hernandez-Lasheras, E. Reyes, E. Heslop, R. Escudier, E. Cutolo, S. Ruiz, E. Mason, A. Pascual, J. Tintore, Assessment of high-resolution regional ocean prediction systems using multi-platform observations: Illustrations in the western Mediterranean Sea, in: E. Chassignet, A. Pascual, J. Tintoré, J. Verron (Eds.), New Frontiers in Operational Oceanography, 2018, Ch. 24, pp. 663–694. doi:10.17125/gov2018.ch24.

[122] NOAA NCEP (National Centers for Environmental Prediction), NOAA/NCEP Global Forecast System (GFS) atmospheric model (Aug. 2023).
URL https://www.emc.ncep.noaa.gov/emc/pages/numerical_forecast_systems/gfs.php

[123] E. Capó, J. C. McWilliams, A. Jagannathan, Flow-topography interaction along the Spanish slope in the Alboran Sea: Vorticity generation and connection to interior fronts, Journal of Geophysical Research: Oceans 128 (4) (2023) e2022JC019480. doi:10.1029/2022JC019480.

[124] P. F. J. Lermusiaux, C.-S. Chiu, G. G. Gawarkiewicz, P. Abbot, A. R. Robinson, R. N. Miller, P. J. Haley, Jr, W. G. Leslie, S. J. Majumdar, A. Pang, F. Lekien, Quantifying uncertainties in ocean predictions, Oceanography 19 (1) (2006) 92–105. doi:10.5670/oceanog.2006.93.

[125] P. F. J. Lermusiaux, Uncertainty estimation and prediction for interdisciplinary ocean dynamics, Journal of Computational Physics 217 (1) (2006) 176–199. doi:10.1016/j.jcp.2006.02.010.

[126] E. P. Chassignet, H. E. Hurlburt, O. M. Smedstad, G. R. Halliwell, P. J. Hogan, A. J. Wallcraft, R. Baraille, R. Bleck, The HYCOM (Hybrid Coordinate Ocean Model) data assimilative system, Journal of Marine Systems 65 (1-4) (2007) 60–83.

[127] E. Clementi, A. Aydogdu, A. C. Goglio, J. Pistoia, R. Escudier, M. Drudi, A. Grandi, A. Mariani, V. Lyubartsev, R. Lecci, S. Cretí, G. Coppini, S. Masina, N. Pinardi, Mediterranean Sea physical analysis and forecast (CMEMS MED-currents, EAS6 system) (version 1), Accessed 2019-04-09 (Feb. 2023). doi:10.25423/CMCC/MEDSEA_ANALYSISFORECAST_PHY_006_013_EAS6.

[128] H. Obermaier, K. I. Joy, Future challenges for ensemble visualization, IEEE Computer Graphics and Applications 34 (03) (2014) 8–11. doi:10.1109/MCG.2014.52.

[129] P. F. J. Lermusiaux, P. J. Haley, Jr., S. Jana, A. Gupta, C. S. Kulkarni, C. Mirabito, W. H. Ali, D. N. Subramani, A. Dutt, J. Lin, A. Shcherbina, C. Lee, A. Gangopadhyay, Optimal planning and sampling predictions for autonomous and Lagrangian platforms and sensors in the northern Arabian Sea, Oceanography 30 (2) (2017) 172–185, special issue on Autonomous and Lagrangian Platforms and Sensors (ALPS). doi:10.5670/oceanog.2017.242.

[130] B. Schnitzler, P. J. Haley, Jr., C. Mirabito, E. M. Mule, J.-M. Moschetta, D. Delahaye, A. Drouin, P. F. J. Lermusiaux, Hazard-time optimal path planning for collaborative air and sea drones, in: OCEANS 2024 IEEE/MTS Halifax, IEEE, Halifax, 2024, pp. 1–10. doi:10.1109/OCEANS55160.2024.10753934.

[131] M. M. N. Robin, P. J. Haley, Jr., C. Mirabito, P. F. J. Lermusiaux, Dynamically-orthogonal parabolic equations for probabilistic ocean acoustics in the New England Seamounts, in: OCEANS 2024 IEEE/MTS Halifax, IEEE, Halifax, 2024, pp. 1–8. doi:10.1109/OCEANS55160.2024.10754458.

[132] P. F. J. Lermusiaux, M. Doshi, C. S. Kulkarni, A. Gupta, P. J. Haley, Jr., C. Mirabito, F. Trotta, S. J. Levang, G. R. Flierl, J. Marshall, T. Peacock, C. Noble, Plastic pollution in the coastal oceans: Characterization and modeling, in: OCEANS 2019 MTS/IEEE SEATTLE, IEEE, Seattle, 2019, pp. 1–10. doi:10.23919/OCEANS40490.2019.8962786.

[133] A. Gupta, P. J. Haley, D. N. Subramani, P. F. J. Lermusiaux, Fish modeling and Bayesian learning for the Lakshadweep Islands, in: OCEANS 2019 MTS/IEEE SEATTLE, IEEE, Seattle, 2019, pp. 1–10. doi:10.23919/OCEANS40490.2019.8962892.

[134] A. Gupta, P. F. J. Lermusiaux, Bayesian learning of coupled biogeochemical-physical models, Progress in Oceanography 216 (2023) 103050. doi:10.1016/j.pocean.2023.103050.